מכון ויצמן למדע
WEIZMANN INSTITUTE OF SCIENCE

Thesis for the degree
Doctor of Philosophy

עבודת גמר (תזה) לתואר
דוקטור לפילוסופיה

Submitted to the Scientific Council of the
Weizmann Institute of Science
Rehovot, Israel

מוגשת למועצה המדעית של
מכון ויצמן למדע
רחובות, ישראל

By
Liron Barak

מאת
לירון ברק

חיפוש ותחזיות לבוזון היגס שמעבר למודל הסטנדרטי
עם הגלאי אטלס במאיץ ההדרונים הגדול

Search and prospects for BSM Higgs with the ATLAS detector at the LHC

Advisor:
Prof. Eilam Gross

מנחה:
פרופ. עילם גרוס

July 2014

תמוז התשע"ד

Contents

Abstract

Almost two years ago, ATLAS [1] and CMS [2] announced the observation of a new boson with a mass of approximately 125 GeV. The properties of this newly discovered boson make a convincing case that it is a Higgs boson related to the BEH mechanism [3–5] of spontaneous breaking of the electroweak (EW) symmetry. Yet, it remains an open question whether it is the Standard Model (SM) Higgs boson, which is a single elementary scalar particle, or one physical state of an extended scalar sector, as predicted by the two-Higgs-doublet-model (2HDM).

There are various ways of trying to answer this exciting question:

- Looking for additional scalar particles (e.g. charged Higgs bosons - light and heavy @ 7-8 TeV). This is the main subject of my thesis.
- Determining the spin/CP quantum numbers.
- Measuring precisely the couplings to fermions and vector bosons.
- Studying additional production mechanisms which are not possible in the SM (e.g. from CP-odd decay).

During my PhD research, I was involved with each of these topics, some of which will only be resolved in a few years time, once ATLAS will collect enough data. In this thesis I review only analyses in which I took a **major** part, from analyzing the 7 TeV data searching for new particles, to studies which make the case for the upgrade of the LHC in general and ATLAS in particular.

Being the main author for the analyses parts which were done by me and described here, some sections of the thesis are taken from the published papers/notes. Some repetition of theoretical parts is kept for clarification of the main issues under the specific research.

1 Introduction

Almost two years ago, the last piece of the Standard Model (SM) was discovered, the Higgs boson [1, 2]. The properties of the new observed particle agree very well with the SM predictions. Even though the BEH mechanism was already suggested 50 years ago, in order to explain how elementary particles acquire their mass [3–5], the Higgs boson, which clearly confirms the mechanism, was only recently discovered (July 2012). This is just the beginning of an exciting experimental period, when many new precision measurements as well as new searches are performed.

This thesis is organized in the following way: This chapter contains general background. Chapter 2 describes the search for the light charged Higgs [6]. In chapter 3 the High-Luminosity (HL) LHC expectations for the SM-Higgs are presented [7], followed by the Beyond the SM (BSM) search for the HL-LHC [8] (chapter 4). Chapter 5 summarizes and concludes the thesis.

1.1 The Standard Model (SM)

As I assume the reader is familiar with the SM [9–11], I only briefly summarize its particle content.

The SM describes the elementary particles and interactions that are currently known and observed experimentally. These include the fermions (quarks and leptons) which have spin $\frac{1}{2}$. Those particles interact through four different types of interactions which are mediated by spin 1(0) particles known as gauge (Higgs) bosons:

- Strong interaction, mediated by the spin 1 massless gluons.
- Weak interaction, mediated by three spin 1 massive particles: $W^{\pm}$ and Z^0.
- Electromagnetic interaction, mediated by the spin 1 massless photon.
- Yukawa interaction (by which fermions acquire mass), mediated by the spin 0 massive Higgs scalar (h).

Quarks interact via all four interactions, charged leptons via all but the strong interaction and neutrinos only via the weak interactions.

Mathematically, the SM is formulated as a gauge theory. One requires that the lagrangian of the theory be invariant under a gauge transformation. The SM gauge group is $SU(3)_c \times SU(2)_W \times U(1)_Y$. The particles in that theory should be massless under that gauge group. Yet, the spin $\frac{1}{2}$ particles, as well as the weak mediators, are massive. That means the the electroweak (EW) gauge symmetry $SU(2)_W \times U(1)_Y$ has to be spontaneously broken. To achieve this, a complex scalar field which is a doublet of $SU(2)_W$ is introduced with a potential given by $V(\phi) = -\mu^2|\phi|^2 + \lambda|\phi|^4$ with $\mu^2, \lambda > 0$ and a minimum at $|\phi|^2 = \frac{\mu^2}{2\lambda}$. The non zero value of the field breaks spontaneously the gauge symmetry and gives masses to the gauge bosons and spin $\frac{1}{2}$ particles through interactions with the scalar field [3–5, 12–14]. The Higgs boson is the physical particle which is associated with the scalar field introduced. Its existence is a solid prediction of the theory.

1.2 Problems of the SM

The SM success in predicting the elementary particle world is ”unfortunately” accurate beyond any expectations. However, there are few issues where the SM fails in the description and there are experimental results which contradict the SM. Some of these problems are listed below.

1.2.1 Neutrino masses

Recent observations of neutrino flavor oscillations probe that the neutrinos are massive [15]. Particulary interesting are the measurements of the solar neutrino flux, which found that although the sun produces only ν_e's, their flux is significantly smaller than the total solar neutrino flux. Also, the flux of atmospheric neutrinos find that the ratio of ν_μ-to-ν_e fluxes is different from expectations. However, in the SM, the neutrinos are massless, this means that the SM must be extended. One popular possibility is the seesaw mechanism [16] which predicts the existence of heavy fermions (singlets of the SM). Note that these heavy fermions won't be easily accessible at the LHC.

1.2.2 Dark matter

In 1932, astrophysicists observed that 4% of the total energy density of the universe consisted of baryonic matter [17]. Now, it appears that nearly 25% of the energy density is due to dark matter, and the remainder is referred to as dark energy. The requirement for dark matter cannot be explained within the SM. However, adding Weakly Interacting Massive Particles (WIMPs) to the SM can solve the problem.

1.2.3 Baryon asymmetry

Cosmological observations from light element abundances and the Cosmic Microwave Background Radiation (CMBR) [18] imply some baryon anti baryon asymmetry which require CP violation. The SM CP violation from the Cabibbo Kobayashi Maskawa (CKM) phase generates a baryon asymmetry that is smaller by at least twelve orders of magnitude than the observed asymmetry. This implies that there are new sources of CP violation, beyond the SM. There are few possibilities for new sources for CP violation, famous examples are Leptogenesis [19] (adding heavy fermions which won't be reachable at the LHC) and Electroweak Baryogenesis which will be tested at the LHC.

1.3 Two-Higgs-Doublet Models (2HDM)

The various shortcoming of the SM require that there is new physics. In most of the SM extensions, there is an extension of the scalar sector to include more than just one doublet (like in the fermionic sector). One of the most popular extensions is the 2HDM and particulary its CP conserving version [20].

One of the most significant constraints on the Higgs sector comes from the observational fact that $\rho \equiv m_W/(m_Z \cos\theta_W) \approx 1$. In general, extensions of the Higgs sector violate this property and thus require a certain level of fine tuned parameters to satisfy the experimental constraints. Extensions of the Higgs sectors that employ SU(2) doublets or singlets [20] satisfy $\rho = 1$ at tree level. The addition of another SU(2) doublet of fields to the Higgs sector is therefore one of the simplest extentions of the SM and defines a large class of models, which are collectively referred to as two-Higgs-doublet models (2HDMs). They also include the minimal supersymmetric SM (MSSM) [21–25]. There are many motivations for 2HDMs. The best known motivation is supersymmetry (SUSY), which provide solution to the dark matter problem. Still another motivation is the ability of 2HDMs to generate a baryon asymmetry of the universe of sufficient size [26, 27].

The most general gauge invariant scalar potential that includes two Higgs doublets, Φ_1 and Φ_2, is given by:

$$V(\Phi_1,\Phi_2) = m_{11}^2\Phi_1^\dagger\Phi_1 + m_{22}^2\Phi_2^\dagger\Phi_2 - (m_{12}^2\Phi_1^\dagger\Phi_2 + \text{h.c}) + \frac{1}{2}\lambda_1(\Phi_1^\dagger\Phi_1)^2 + \frac{1}{2}\lambda_2(\Phi_2^\dagger\Phi_2)^2 + \lambda_3(\Phi_1^\dagger\Phi_1)(\Phi_2^\dagger\Phi_2)$$
$$+\lambda_4(\Phi_1^\dagger\Phi_2)(\Phi_2^\dagger\Phi_1) + \left\{\frac{1}{2}\lambda_5(\Phi_1^\dagger\Phi_2)^2 + [\lambda_6(\Phi_1^\dagger\Phi_1) + \lambda_7(\Phi_2^\dagger\Phi_2)](\Phi_1^\dagger\Phi_2) + \text{h.c}\right\} \quad (1.3.1)$$

With EW symmetry breaking, there are five physical scalars: two CP-even bosons, h and H (defined such that $m_h < m_H$), one CP-odd particle A and two charged scalar particles $H^\pm$.

The Yukawa couplings of the two Higgs doublets are such that tree level flavour changing neutral currents can be avoided by imposing a discrete $\mathcal{Z}_2$ symmetry: $\Phi_1 \to -\Phi_1$. In the following, a potential with only soft breaking terms for such a symmetry is considered, i.e. $\lambda_6 = \lambda_7 = 0$. In addition, CP-symmetry conservation is assumed, from which it follows that all potential parameters are real numbers.

The potential of Eq 1.3.1 has 8 parameters after imposing the softly broken $\mathcal{Z}_2$ symmetry and CP-conservation. These can be expressed in terms of (1) the masses of the bosons, m_h, m_H, m_A, $m_{H^\pm}$, (2) the ratio of the vacuum expectation values of the two doublets: $\tan\beta \equiv \upsilon_2/\upsilon_1$, where $\upsilon_1 \equiv <\Phi_1>_0$ and $\upsilon_2 \equiv <\Phi_2>_0$, (3) the mixing angle between the CP-even bosons, α and (4) the m_{12}^2 potential parameter[1]. It is always possible to adjust the phases of the two doublets such that both υ_1 and υ_2 are positive, hence the angle β can be chosen to be $0 < \beta < \pi/2$. In the following, by convention, the sign of α is defined such that $-1 \leq \cos(\beta-\alpha) \leq 1$ and $\sin(\beta-\alpha) \geq 0$.

An additional freedom of the model is the exact form of the $\mathcal{Z}_2$ symmetry in the Yukawa sector of the Lagrangian. Type-I 2HDMs are defined with a $\mathcal{Z}_2$ symmetry $\Phi_1 \to -\Phi_1$. Similarly, type-II 2HDMs are defined by choosing the $\mathcal{Z}_2$ symmetry to be $\Phi_1 \to -\Phi_1$,

[1]The additional 8th parameter that appears in the potential is removed by using the relation $\upsilon_1^2 + \upsilon_2^2 = \upsilon^2$, where $\upsilon = 246$ GeV is equivalent to the vacuum expectation value of the Higgs doublet in the SM.

$d_R \to -d_R$, where the notation d_R refers to the right-handed down type fermions. In practice, this means that in a type-I 2HDM all fermions[2] couple only to Φ_2, whereas in type-II models, up-type right-handed fermions couple to Φ_2 and down-type right-handed fermions to Φ_1.

We define the parameters $\xi_h^f, \xi_H^f, \xi_A^f$ through the Yukawa Lagrangian for the resulting Yukawa interactions of the five physical scalars:

$$\mathcal{L}_{Yukawa}^{\text{2HDM}} = -\sum_f \frac{m_f}{v}(\xi_h^f \bar{f} f h + \xi_H^f \bar{f} f H - i\xi_A^f \bar{f}\gamma_5 f A)$$

$$-H^+(\frac{\sqrt{2}V_{ud}}{v}\bar{u}(m_u \xi_A^u P_L + m_d Y \xi_A^d P_R)d + \frac{\sqrt{2}m_l}{v}\xi_A^l \bar{\nu_L} l_R) + H.C \tag{1.3.2}$$

where $P_{L/R}$) are projection operators for left-/right-handed fermions, and the factors ξ are presented in Table 1.3.1.

In all 2HDMs that are discussed here, the couplings of h and H to the vector bosons are the same as the SM couplings of the Higgs boson times $\sin(\beta - \alpha)$ and $\cos(\beta - \alpha)$, respectively, whereas for A these couplings vanish. The couplings of the type-I and type-II 2HDMs with respect to the SM Higgs couplings are shown in Table 1.3.1. In the following the mixing angle α only appears as $\sin(\beta - \alpha)$ or $\cos(\beta - \alpha)$ due the easier interpretation of these combinations. The SM-like limit of the 2HDM is defined as the regime in which $\sin(\beta - \alpha) \to 1$. In this limit the couplings of the lightest CP-even Higgs boson, h, are the same as for the SM Higgs boson.

As for the charged Higgs in the models described above, the most general Yukawa couplings can be written as

$$\mathcal{L}_{H^+} = -H^+(\frac{\sqrt{2}V_{ud}}{v}\bar{u}(m_u \xi_A^u P_L + m_d Y \xi_A^d P_R)d + \frac{\sqrt{2}m_l}{v}\xi_A^l \bar{\nu_L} l_R) + H.C \tag{1.3.3}$$

where $\xi_A^{u,d,l}$ are the same as in Table 1.3.1.

The MSSM Higgs sector is a type-II 2HDM at the tree level [28]. The general discussion about the couplings and the production mechanisms made previously for type-II 2HDMs are therefore valid also in this case. When introducing the MSSM, at tree level, most of the free parameters of the Higgs potential are fixed, leaving (m_A, $\tan\beta$) as the two free parameters. Radiative corrections due to the supersymmetric particles are specific to the MSSM scenario.

[2] In this section, "all fermions" means all SM fermions excluding neutrinos.

	type-I	type-II
ξ_h^u	$\sin(\beta-\alpha)+\cos(\beta-\alpha)/\tan\beta$	$\sin(\beta-\alpha)+\cos(\beta-\alpha)/\tan\beta$
ξ_h^d	$\sin(\beta-\alpha)+\cos(\beta-\alpha)/\tan\beta$	$\sin(\beta-\alpha)-\cos(\beta-\alpha)\cdot\tan\beta$
ξ_h^l	$\sin(\beta-\alpha)+\cos(\beta-\alpha)/\tan\beta$	$\sin(\beta-\alpha)-\cos(\beta-\alpha)\cdot\tan\beta$
ξ_H^u	$\cos(\beta-\alpha)-\sin(\beta-\alpha)/\tan\beta$	$\cos(\beta-\alpha)-\sin(\beta-\alpha)/\tan\beta$
ξ_H^d	$\cos(\beta-\alpha)-\sin(\beta-\alpha)/\tan\beta$	$\cos(\beta-\alpha)+\sin(\beta-\alpha)\cdot\tan\beta$
ξ_H^l	$\cos(\beta-\alpha)-\sin(\beta-\alpha)/\tan\beta$	$\cos(\beta-\alpha)+\sin(\beta-\alpha)\cdot\tan\beta$
ξ_A^u	$1/\tan\beta$	$1/\tan\beta$
ξ_A^d	$-1/\tan\beta$	$\tan\beta$
ξ_A^l	$-1/\tan\beta$	$\tan\beta$

Table 1.3.1: Yukawa coupling coefficients of the neutral boson of the type-I and type-II 2HDMs for up-type quarks (u), down-type quarks (d) and charged leptons (l).

1.4 The LHC

In 2010, at the European Center for Nuclear Research (CERN) in Geneva, Switzerland, the Large Hadron Collider (LHC) provided its first pp collisions at a beam energy of 3.5 TeV. The LHC is the highest energy hadron accelerator and collider facility in the world, designed to ultimately provide proton-proton collisions at an center-of-mass energy of $\sqrt{s} = 14$ TeV. It is located approximately 100 m underground in a 27 km circumference tunnel. The acceleration process occurs in several stages. First, linear accelerator (Linac2) accelerates protons to 50 MeV for injection into the Proton Synchrotron Booster. After that, a series of circular synchrotrons take on: the Proton Synchrotron Booster brings their energy up to 1.4 GeV, the Proton Synchrotron accelerates them further up to 26 GeV, and after the Super Proton Synchrotron they reach an energy of 450 GeV [29]. Finally they go into the main synchrotron in the 27 km long LHC tunnel. This complex accelerates protons from rest to the current maximum energy of 4 TeV.

At the end of Run 1, the protons were collided at 8 TeV while the goal energy of the LHC is 14 TeV with a luminosity of $10^{34} cm^{-2} s^{-1}$ [29]. In order to accelerate protons to such energies in a circular accelerator a magnetic field of 8.3 Tesla is required. Superconducting bending magnets operating at 1.9 K are used to produce this field in order to have a reasonable power consumption. The proton bunches are spaced 25 ns apart.

1.4.1 ATLAS Detector

The ATLAS detector is described elsewhere [30], here, only a brief outline is presented. ATLAS is one of the two general purpose detectors at the LHC. The coordinates used are ϕ and η. ϕ is the azimuthal angle (where the x-y plane is the plane perpendicular to the beam pipe) and $\eta = ln(\tan\frac{\theta}{2})$ where θ is the polar angle. η is used instead of θ because differences in η between massless particles are invariant under Lorentz Boosts in the Z direction.

It consists of an inner detector immersed in a 2 T solenoidal field. A combination of high resolution silicon made pixel and strip detectors, together with straw tube tracking detectors, achieve the pattern recognition, momentum and vertex measurements, as well as electron identification up to $|\eta| \leq 2.51$. The ATLAS calorimeter in the barrel is composed of high granularity Liquid Argon (LAr) electromagnetic sampling calorimeters that cover the pseudorapidity range up to $|\eta| \leq 3.2$. The hadronic calorimeter in the barrel is made of scintillating tiles and covers the range $|\eta| \leq 1.7$. In the range $|\eta| \geq 1.5$, namely the end-caps, the hadronic calorimeter uses LAr technology. At higher $|\eta|$, up to $|\eta| \leq 4.9$, LAr is used for both electromagnetic (EM) and hadronic (HAD) energy measurements. The ATLAS muon system is based on an air core toroid system which gives ATLAS its name (A Toroidal LHC Apparatus) and typical look, and also minimizes multiple scattering, thus achieving excellent muon momentum resolution. The muon system includes four different technologies: the Monitored Drift Tubes (MDT) cover the range $|\eta| \leq 2.7$, the Cathode Strip Chambers (CSC) cover the range $2.0 \leq |\eta| \leq 2.7$, the Resistive Plate Chambers (RPC) cover the range $|\eta| \leq 1.05$, and the Thin Gap Chambers (TGC) cover the range $1.05 \leq \eta \leq 2.7$ (2.4 for triggering). The muon system trigger capabilities have a timing resolution of the order of 1.5-4 ns.

2 Search for light Charged Higgs

This chapter covers a search for charged Higgs bosons in the ATLAS experiment, based on 4.6 fb^{-1} of proton-proton collision data at $\sqrt{s} = 7$ TeV using the lepton+jets channel in $t\bar{t}$ decays with a leptonically decaying τ in the final state. The data agree with the Standard Model expectation. Assuming $\mathcal{B}(H^+ \to \tau\nu) = 1$, this leads to upper limits on the branching fraction $\mathcal{B}(t \to bH^+)$ between 4% and 15% for charged Higgs boson masses (m_{H^+}) in the range $90GeV < m_{H^+} < 160GeV$. In the context of the m_h^{max} scenario of the MSSM, values of $\tan\beta$ larger than 27–44 are excluded for charged Higgs boson masses in the range $90GeV < m_{H^+} < 140GeV$. This analysis was performed by me and has already been published [6] together with the complementary channels, hadronically decaying τ, in the final state.

This chapter is organized in the following way: Section 2.2 describes the discriminating variables used in the analysis. In Section 2.3, the Monte Carlo and data samples used for this study are summarised. In Section 2.4, the reconstruction of physics objects in ATLAS is described and, in Section 2.5, a data-driven method aimed at deriving the contribution of backgrounds with misidentified leptons is presented. Section 2.6 deals with the measurement of $\cos\theta_l^*$ and the transverse mass m_{T}^H in ATLAS data and Monte Carlo simulated events, based on a lepton+jets $t\bar{t}$ event topology. Assuming $\mathcal{B}(H^+ \to \tau\nu) = 1$, upper limits on the branching fraction $\mathcal{B}(t \to bH^+)$ at the 95% confidence level are presented (Section 2.7). Finally, a summary is given in Section 2.8.

All the analysis in this chapter was done by me except for the estimation of fake leptons (Section 2.5) which was done in collaboration with Jacob Groth-Jensen.
The analysis was published in [6].

2.1 Introduction

Charged Higgs bosons, H^+ and H^-, are predicted by several non-minimal Higgs scenarios [31, 32], such as models containing Two-Higgs-Doublet Models (2HDM) [33]. The observation of a charged Higgs boson[3] would therefore clearly indicate new physics beyond the Standard Model (SM).

In a type-II 2HDM, which is also the Higgs sector of the Minimal Supersymmetric Standard Model (MSSM) [28], for charged Higgs boson masses smaller than the top quark mass ($m_{H^+} < m_{\text{top}}$), the main H^+ production mode at the Large Hadron Collider (LHC) is through the top quark decay $t \to bH^+$. The dominant source of top quarks at the LHC is through $t\bar{t}$ production. However, as the mass of H^+ reach the mass of the top, interference effects from the top association production can be enlarged, thus, the search was limited to up to 160 GeV.

The main decay modes of the charged Higgs boson, which are accessible experimentally, are into $\tau\nu$ and $c\bar{s}$ (Eq 1.3.3). The $c\bar{b}$ decay can be dominant in part of the parameter space, but from experimental reasons, that was not consider. The charged Higgs couples to the heaviest lepton, which is the τ lepton, with an enhanced strength proportional to $\tan\beta$. In the quark sector, the heaviest quark which is kinematically available for light charged Higgs, is the Charm quark, but its coupling is suppressed by $\frac{1}{\tan\beta}$. The $\tau\nu$ decay mode is therefore the dominant one [34].

In this analysis, $\mathcal{B}(H^+ \to \tau\nu) = 1$ is always assumed. For this assumption, the combined LEP lower limit for the charged Higgs boson mass (based on the direct search for Drell-Yan production) is about 90 GeV [35]. At the Tevatron, no evidence for charged Higgs boson production in $p\bar{p}$ collisions has been found. Hence, the Tevatron experiments placed model dependent upper limits in the 15–20% range on $\mathcal{B}(t \to bH^+)$ [36, 37]. In addition, preliminary results of charged Higgs boson searches in top quark decays, based on about 1 fb^{-1} of LHC collision data at $\sqrt{s} = 7$ TeV, have been made public by the CMS experiment [38], and also by ATLAS in the $t\bar{t} \to b\bar{b}WH^+ \to b\bar{b}qq'\tau_{\text{had}}\nu$ channel [39], as well as for $t\bar{t}$ events with a leptonically decaying τ in the final state [40].

This chapter describes in detail the search for charged Higgs bosons in $t\bar{t}$ events with the topology shown in Fig. 2.1.1, and in particular one leptonically decaying τ and jets in the final state, using data from proton-proton collisions at $\sqrt{s} = 7$ TeV, collected in 2011 with the ATLAS experiment [30] at the LHC.

[3] In the following, charged Higgs bosons will be denoted H^+, with the charge-conjugate H^- always implied.

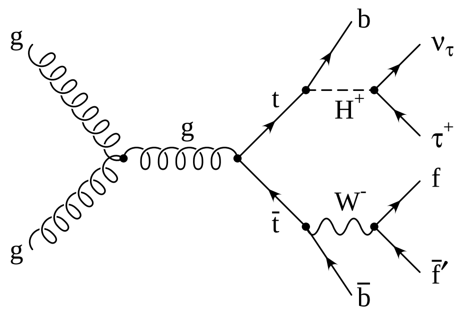

Figure 2.1.1: Example of a leading-order Feynman diagram for the production of a charged Higgs boson in $t\bar{t}$ events arising from gluon fusion.

2.2 The discriminating variables

If the charged Higgs boson solely decays into $\tau\nu$, then a small increase in the branching fraction for lepton+jets[4] decays of $t\bar{t}$ pairs occurs, because the τ decays leptonically more often than the W boson: $\mathcal{B}(H^+ \to \tau\nu \to l + N\nu) \simeq 35\%$ while $\mathcal{B}(W \to l + N\nu) \simeq 25\%$. However, viable search strategies for charged Higgs bosons do not only rely on the presence or absence of an excess of lepton+jets $t\bar{t}$ events, as compared to the SM predictions. In addition, it is useful to identify discriminating variables that allow distinction between leptons produced in $\tau \to l\nu_l\nu_\tau$ (e.g. in decays of W or charged Higgs bosons) and leptons arising directly from W boson decays.

One such discriminating variable is the invariant mass m_{bl} of a b quark and a light charged lepton l (electron or muon) coming from the same top quark, or more conveniently $\cos\theta_l^*$ defined as:

$$\cos\theta_l^* = \frac{2m_{bl}^2}{m_{\text{top}}^2 - m_W^2} - 1 \simeq \frac{4\,p^b \cdot p^l}{m_{\text{top}}^2 - m_W^2} - 1 \text{ with } p^b \cdot p^l = 2E_bE_l(1 - \cos\theta_{bl}) = 4E_bE_l\sin^2(\theta_{bl}/2), \tag{2.2.1}$$

where p^b and p^l are the four-momenta of the b quark and of the charged lepton l (they can be chosen in any reference frame, since $\cos\theta_l^*$ contains an invariant product) and θ_{bl} is the angle between them. Note that both m_b^2 and m_l^2 are neglected, hence $m_{bl}^2 \simeq 2\,p^b \cdot p^l$.

[4]In the following, if not otherwise specified, "leptons" l refer to electrons and muons.

This variable is commonly used to measure the polarisation of W bosons in top quark decays [41], in which case θ_l^* is the angle of the lepton momentum with respect to the helicity axis in the W rest frame. In this analysis, the same variable $\cos\theta_l^*$ is used for other purposes. Indeed, if a top quark decay is mediated through an H^+ and if the H^+ is heavier than the W boson, the b quark usually has a smaller momentum than in the case of a W-mediated top quark decay. Also, a charged lepton l arising from a τ decay is likely to have a smaller momentum than a lepton coming directly from a on-shell W boson. As a result, the presence of a charged Higgs boson in a leptonic top quark decay strongly reduces the invariant product $p^b \cdot p^l$, leading to $\cos\theta_l^*$ values mostly close to -1, as illustrated by Fig. 2.2.1.

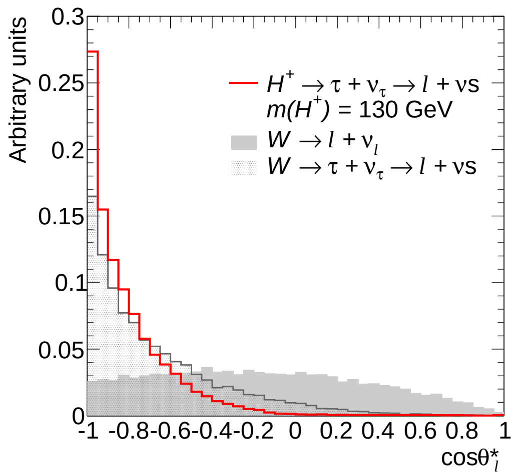

Figure 2.2.1: Effect of the presence of a charged Higgs boson in the leptonic decay of a top quark on the $\cos\theta_l^*$ distribution, at generator level. A correct assignment of all top quark decay products is assumed. The grey histograms show the $\cos\theta_l^*$ distributions with unit area expected in the SM and the red histogram shows the $\cos\theta_l^*$ distribution with unit area for $t \to bH^+$, assuming $m_{H^+} = 130$ GeV.

A new transverse mass observable is also introduced, which can help discriminate leptons produced in $H^+ \to \tau\nu$ decays from leptons coming from W bosons [42]. In lepton+jets $t\bar{t}$ events where a W boson decays directly into an electron or muon and one neutrino, the W transverse mass is obtained by minimising $(p^l + p^{\text{miss}})^2$ while constraining the (squared) missing mass $(p^{\text{miss}})^2$ to be zero, assuming that it only comes from the massless neutrino associated with the direct W decay:

$$(m_{\mathrm{T}}^{W})^2 = \min_{\left\{\substack{p_z^{\mathrm{miss}},\,E^{\mathrm{miss}} \\ (p^{\mathrm{miss}})^2\,=\,0}\right\}} [(p^l + p^{\mathrm{miss}})^2] = 2{P_T}^l E_T^{miss}(1 - \cos\phi_{l,\mathrm{miss}}). \tag{2.2.2}$$

Here, p_z^{miss} and E^{miss}, i.e. the longitudinal momentum and the energy of the neutrino, are varied, ${P_T}^l$, E_T^{miss} and $\phi_{l,\mathrm{miss}}$ being the transverse momenta of the lepton and the neutrino, as well as the azimuthal angle between them, respectively. In the case of a leptonic τ decay (either from a W or charged Higgs boson), the missing momentum comes from three neutrinos, hence $(p^{\mathrm{miss}})^2 \neq 0$. However, if one of the two b quarks can be associated with the leptonically decaying top quark, one can compute the *charged Higgs boson transverse mass* by performing a maximisation of the invariant mass $(p^l + p^{\mathrm{miss}})^2$ while requiring $(p^{\mathrm{miss}}+p^l+p^b)^2 = m_{\mathrm{top}}^2$, now varying the longitudinal momentum and energy of all neutrinos (again referred to as p_z^{miss} and E^{miss}):

$$(m_{\mathrm{T}}^{H})^2 = \max_{\left\{\substack{p_z^{\mathrm{miss}},\,E^{\mathrm{miss}} \\ (p^{\mathrm{miss}}+p^l+p^b)^2=m_{\mathrm{top}}^2}\right\}} [(p^l + p^{\mathrm{miss}})^2]. \tag{2.2.3}$$

The explicit expression of the charged Higgs boson transverse mass is:

$$(m_{\mathrm{T}}^{H})^2 = \left(\sqrt{m_{\mathrm{top}}^2 + ({\vec{P}_T}^{\,l} + {\vec{P}_T}^{\,b} + {\vec{P}_T}^{\,\mathrm{miss}})^2} - {P_T}^b\right)^2 - \left({\vec{P}_T}^{\,l} + {\vec{P}_T}^{\,\mathrm{miss}}\right)^2. \tag{2.2.4}$$

Figure 2.2.2 shows the m_{T}^{H} distribution at generator level , obtained in the SM or assuming the presence of a 130 GeV charged Higgs boson in the top quark decay. At first order, this transverse mass is larger than the true charged Higgs boson mass m_{H^+} and smaller than the top quark mass used in the constraints, m_{top}.

2.3 Monte Carlo samples and data

Monte Carlo samples intended for the analysis of the 2011 data are provided by the MC11 campaign of the ATLAS production group. The sample statistics of the MC11 production round are such that the statistical uncertainties obtained when working with the Monte Carlo simulated samples remain smaller than those obtained when working with the 2011 data sample. In this study, the estimation of the multi-jet background is only performed with data-driven techniques, therefore none of the QCD Monte Carlo samples is used here.

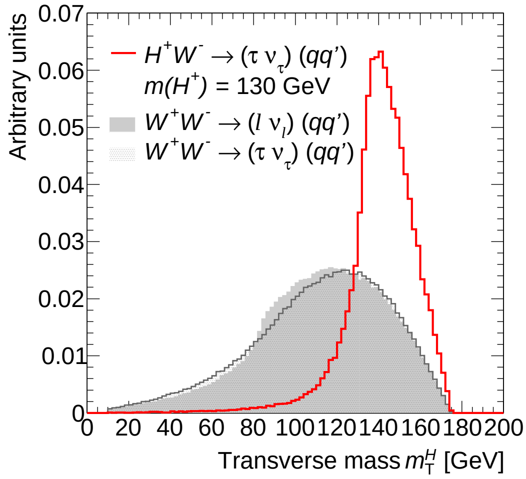

Figure 2.2.2: Effect of the presence of a charged Higgs boson on the transverse mass m_{T}^{H}, at generator level. A correct assignment of all top quark decay products is assumed. The grey histograms show the m_{T}^{H} distributions with unit area expected in the SM and the red histogram shows the m_{T}^{H} distribution with unit area for $t \to bH^+$, assuming $m_{H^+} = 130$ GeV.

The modeling of the $t\bar{t}$ and single top quark events is performed with MC@NLO [43], except for the t-channel of the single quark production, in which case AcerMC [44] is used. The top quark mass is set to 172.5 GeV and the parton density function is CT10 [45]. The parton shower and the underlying event are added using HERWIG [46] and JIMMY [47] for events generated with MC@NLO. PYTHIA [48] is instead used for events generated with AcerMC. The (inclusive) $t\bar{t}$ production cross section is normalised to the approximate next-to-next-to-leading order (NNLO) prediction of 167 pb [49]. For the single top quark production, approximate NNLO calculations are used for the (inclusive) cross sections, i.e. 64.6 pb, 4.6 pb and 15.7 pb for the t-, s- and Wt-production channels, respectively [50–52]. Single top quark events are available for each of the leptonic (e, μ and τ) t- and s-channels and for the inclusive Wt-channel. Overlaps between single top quark and $t\bar{t}$ final states are removed [53].

Various $t\bar{t}$ samples using other generators and parameter setups are also available. For instance, $t\bar{t}$ samples simulated using POWHEG [54], interfaced with PYTHIA or HERWIG/JIMMY, allow the comparison of two different parton shower and hadronisation models. For initial and final state radiation studies, a set of $t\bar{t}$ samples, generated with AcerMC and PYTHIA, is available. The initial and final state parameters (or their combinations) are set to a range of values not excluded by current data.

Single vector boson production is simulated using ALPGEN interfaced to HERWIG/JIMMY for the underlying event model. The parton density function CTEQ6.1 [55] is used for both matrix element calculations and parton shower evolution. The additional partons produced in the matrix element part of the event generation can be light partons or heavy quarks[5]. The ALPGEN parameters controlling the minimal transverse momentum and angular separation of the light quarks are set to ptjmin = 15 GeV and drjmin = 0.7. The MLM matching [56] is applied inclusively for the production of W + 5 partons and exclusively for the lower multiplicity sub-samples. The clustering parameters of the MLM matching are set to RCLUS = 0.7 and ETCLUS = 20 GeV. The production cross sections of all samples are rescaled by 1.20 and 1.25, respectively, in order to match NNLO calculations [57, 58].

Diboson events (WW, WZ and ZZ) are generated and hadronised using HERWIG. For these events, inclusive decays are used for both gauge bosons, and a filter is applied at the generator level, requiring at least one electron or muon with $P_T > 10$ GeV and a pseudorapidity $|\eta| < 2.8$. Similarly to the single vector boson production, the cross sections are rescaled (by 1.48 for WW, 1.60 for WZ, and 1.30 for ZZ) to match next-to-leading order predictions [59].

Finally, three types of signal samples are produced with PYTHIA for m_{H^+} between 90 and 160 GeV: $t\bar{t} \to b\bar{b}H^+W^-$, $t\bar{t} \to b\bar{b}H^-W^+$ and $t\bar{t} \to b\bar{b}H^+H^-$, where the charged Higgs bosons decay as $H^+ \to \tau\nu$. When a top quark decays into Wb, the W boson subsequently decays inclusively. TAUOLA [60] is used for τ decays, and PHOTOS [61] is used for photon radiation from charged leptons.

Event generators are tuned in order to describe the ATLAS data. The parameter sets AUET2B [62] and AUET2 [63] are used for events hadronised with PYTHIA and HERWIG/JIMMY, respectively. The SM background and signal samples used in this study are summarised in Tables 2.3.1 and 2.3.2, respectively. All Monte Carlo events are propagated through a detailed GEANT4 simulation [64, 65] of the ATLAS detector, and they are reconstructed with the same algorithms as the data. Only events recorded with all ATLAS sub-

[5]The Heavy Flavor Overlap Removal (HFOR) tool is used to deal with heavy flavor final states arising in multiple samples.

systems fully operational are used for this analysis. Together with the requirement of having 7 TeV pp collisions with stable beams, this results in a 2011 data sample of 4.6 ± 0.2 fb^{-1}, i.e. with an uncertainty of 3.9% [66].

Process	Generator	Sample(s)	Cross section (pb)
$t\bar{t}$ with at least one lepton ℓ	MC@NLO	105200	90.6
$t\bar{t}$ with no lepton	MC@NLO	105204	76.2
Single top quark t (with ℓ)	AcerMC	117360–2	20.9
Single top quark s (with ℓ)	MC@NLO	108343–5	1.5
Single top quark Wt (inclusive)	MC@NLO	108346	15.7
$W(\ell\nu)$ + jets	ALPGEN	107680–5 ($e\nu$) 107690–5 ($\mu\nu$) 107700–5 ($\tau\nu$)	3.1×10^4
$Wb\bar{b}$ + jets	ALPGEN	107280–3	1.3×10^2
$Z/\gamma^*(\ell\ell)$ + jets, $m(\ell\ell) > 10$ GeV	ALPGEN	107650–5 + 116250–5 (ee) 107660–5 + 116260–5 ($\mu\mu$) 107670–5 + 116270–5 ($\tau\tau$)	1.5×10^4
$Z/\gamma^*(\ell\ell)b\bar{b}$ + jets, $m(\ell\ell) > 30$ GeV	ALPGEN	109300–3 (ee) 109305–8 ($\mu\mu$) 109310–3 ($\tau\tau$)	38.7
WW	HERWIG	105985	17.0
ZZ	HERWIG	105986	1.3
WZ	HERWIG	105987	5.5

Table 2.3.1: Cross sections and dataset ID numbers for the main SM Monte Carlo samples. In this table, ℓ refers to the three lepton families e, μ and τ.

The LHC peak luminosity exceeded 10^{33} cm^{-2}s^{-1} for most of the 2011 data-taking period, a level at which more than one interaction per bunch crossing occurs (on average, 6.3 and 11.6, respectively before and after the September 2011 technical stop, during which the β^*-value was reduced from 1.5 to 1.0 m). In addition, the LHC ran with an in-train bunch separation of 50 ns. Thus, the out-of-time pile-up (i.e. overlapping signals in the detector

m_{H^+} (GeV)	Dataset ID number		
	$t\bar{t} \to b\bar{b}H^+W^-$	$t\bar{t} \to b\bar{b}H^-W^+$	$t\bar{t} \to b\bar{b}H^+H^-$
90	116970	128120	116980
100	116971	128121	116981
110	116972	128122	116982
120	116973	128123	116983
130	116974	109851	116984
140	116975	128125	116985
150	116976	109850	116986
160	116977	128127	116987

Table 2.3.2: Dataset ID numbers for the charged Higgs boson Monte Carlo samples.

from other neighboring bunch crossings) is also very important. For the pile-up simulation, minimum bias events are generated with PYTHIA, assuming variable pile-up rates, and added to the hard process in each Monte Carlo event. Prior to the analysis, the simulated events are reweighted to match the distribution of the average number of pile-up interactions $\langle\mu\rangle$ in the data. As an illustration of the pile-up reweighting procedure, Fig. 2.3.1 shows the normalised distribution of the number of (primary or pile-up) vertices with five or more tracks, in data and in a $t\bar{t}$ Monte Carlo sample, before and after pile-up reweighting.

2.4 Object reconstruction in ATLAS

The ATLAS detector [30] consists of an inner tracking detector with an acceptance $|\eta| < 2.5$ surrounded by a thin 2 T superconducting solenoid, a calorimeter system extending up to $|\eta| = 4.9$ that uses a variety of technologies to detect electrons, photons and hadronic jets, as well as a large muon spectrometer using superconducting toroids arranged with an eight-fold azimuthal coil symmetry.

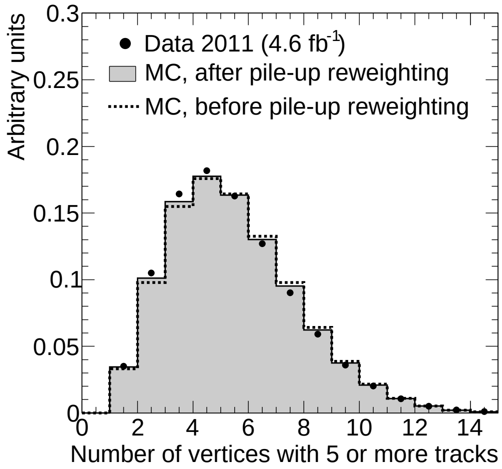

Figure 2.3.1: Normalised distribution of the number of vertices with five or more tracks, in data and in a $t\bar{t}$ Monte Carlo sample, before and after pile-up reweighting of the simulated events.

2.4.1 Data quality

Following the basic data quality checks, further event cleaning is performed by discarding events where any jet with $P_T > 20$ GeV fails the quality cuts discussed in Ref. [67]. This ensures that no jet in the event is consistent with having originated from instrumental effects, such as spikes in the hadronic end-cap calorimeter, coherent noise in the electromagnetic calorimeter, or non-collision backgrounds. In addition, events are discarded if the primary vertex (i.e. with the largest sum of track momenta) has less than five associated tracks.

In order to cope with the failure of six front-end boards in the Liquid Argon (LAr) barrel calorimeter during the periods E–H of the 2011 data, events with a calorimeter jet in the vicinity of this "LAr hole" are discarded. This veto is applied together with the jet cleaning, if an electron or a jet with E_T larger than 15 or 20 GeV, respectively, satisfies $0.1 < \eta < 1.5$ and $-0.5 < \phi < -0.9$.

2.4.2 Trigger

The analysis presented here relies on events passing a single-lepton trigger, with a P_T threshold at 20 or 22 GeV for the electron trigger (`EF_e20_medium` for periods B–H, `EF_e22_medium` for periods I–K and `EF_e22vh_medium1` for periods L–M) and at 18 GeV for the muon trigger (`EF_mu18` for periods B–H and `EF_mu18_medium` for periods I–M). These thresholds are low enough to guarantee that electrons with $E_{\rm T} > 25$ GeV and muons with $P_T > 20$ GeV are in the plateau region of the trigger-efficiency curve.

2.4.3 Electrons

Reconstructed offline electron candidates are selected from `ElectronAODCollection`, with author 1 or 3. A set of quality requirements is then applied in order to ensure consistency with the energy deposition of an electron in the calorimeters and to make sure that there is a well measured track associated with, and matching to, the electromagnetic cluster. These electron quality requirements are enclosed in the definition of `ElectronTight++` with an overall efficiency in the range 70–80% when electrons are additionally requested to have $E_{\rm T} > 20\ GeV$, where $E_{\rm T} = E_{clus}/\cosh(\eta_{track})$ is computed using the calorimeter cluster energy E_{clus} and the direction of the electron track η_{track}. The pseudorapidity range for the electromagnetic cluster is $|\eta_{clus}| < 2.47$ (the transition region between the barrel and end-cap calorimeters, i.e. $1.37 < |\eta_{clus}| < 1.52$, is excluded). Only isolated electrons are considered. For this purpose, various E_T- and η-dependent requirements are imposed in a cone with a radius[6] $\Delta R = 0.2 - 0.3$ around the electron position, excluding the electron object itself, leading to an efficiency of about 90% for true electrons. The efficiencies of the electron trigger, reconstruction and identification are measured using $Z \to ee$ and $W \to e\nu$ events, in both data and Monte Carlo samples. Monte Carlo simulations are generally found to model the data well, with a few exceptions mainly regarding the lateral development of showers and the TRT in the end-caps. Scale factors are derived to parametrise efficiency differences between data and simulations.

2.4.4 Muons

Objects are considered as muon candidates if an inner detector track matches a track reconstructed in the muon spectrometer. Muons contained in `MuidMuonCollection` are considered. More explicitely, combined and tight muons (i.e. with author 12), with a good

[6] $\Delta R = \sqrt{(\Delta\eta)^2 + (\Delta\phi)^2}$, where $\Delta\eta$ is the difference in pseudorapidity of the two objects in question, and $\Delta\phi$ is the difference between their azimuthal angles.

track quality, are selected. An offline reconstructed transverse momentum $P_T > 15$ GeV is requested for the muon candidates, together with $|\eta| < 2.5$. To reduce the contribution of muons reconstructed in jets, only isolated muons are accepted by requiring that, in a cone of radius $\Delta R = 0.2$ (0.3) around the muon, the transverse energy deposited in the calorimeters (the transverse momentum of the inner detector tracks) amounts to less than 4 GeV (2.5 GeV). The energy and momentum of the muon are excluded from the cone when making the isolation requirements. When a muon candidate shares the same inner detector track as a selected electron, the full event is discarded. As in the case of electrons, scale factors are applied to simulated events with muons to account for trigger and identification efficiency differences between data and simulations.

2.4.5 Jets

Jets are reconstructed using the anti-k_t algorithm [68,69], with a size parameter value $\Delta R = 0.4$, from topological clusters in the calorimeter, reconstructed at the electromagnetic scale appropriate for the energy deposited by electrons or photons. Jets are then calibrated with Monte Carlo based P_T- and η-dependent correction factors to restore the full hadronic energy scale after passing through the non-compensating calorimeters [70]. A method originally developed by the D0 collaboration [71] allows identification and selection of the jets originating from the hard-scatter interaction through the use of tracking and vertexing information. By combining the tracks and their primary vertices with calorimeter jets, a discriminant which measures the probability that a jet originated from a particular vertex can be defined, the Jet Vertex Fraction (JVF). Jet selection based on this discriminant is shown to be insensitive to the contributions from simultaneous uncorrelated soft collisions that occur due to pile-up.

The high-performance tagger MV1 [72], combining impact-parameter information with the explicit determination of an inclusive secondary vertex, is used. The cut point gives an efficiency of about 70% (corresponding to a weight $w_{\mathrm{MV1}} > 0.60$) to select b-tagged jets among all jets passing the reconstruction criteria discussed above. As b-tagging relies on the inner tracking detectors, the acceptance region must be restricted to $|\eta| < 2.5$. The performance estimates of the b jet taggers are derived from specific data samples. While the performance of b-tagging algorithms ideally depends on the jet properties only and should be independent of any other specific event properties, this is unlikely to be true in reality.

On the other hand, such dependencies should be properly described in simulated samples. Tagging and mis-tag efficiency scale factors relate efficiencies as determined in various data samples to their counterparts in Monte Carlo samples. These scale factors are then used in the Monte Carlo simulations, after having applied the actual tagging algorithm to the jets.

In order to reconstruct τ jets [73], all anti-k_t jets depositing at least $E_T > 10$ GeV in the calorimeter are considered as candidates. Dedicated algorithms, `tau_EleBDTMedium` and `tau_muonVeto`, are then used in order to reject electrons and muons, respectively. Only candidates with one or three associated tracks reconstructed in the inner detector are considered. Hadronic τ decays are identified using a likelihood quality criterion. The cut point `tau_tauLlhTight` gives an efficiency of about 30% for a τ with $P_T > 20$ GeV in $Z \to \tau\tau$ events and a rejection factor of about 100–1000 for quark- and gluon-initiated jets, depending on the P_T and η of the τ jet, as wel as the number of associated tracks. The τ jets are required to have a visible transverse momentum of at least 20 GeV and to be within $|\eta| < 2.3$.

The following overlap removal procedure is applied. First, muon candidates are rejected if they are found within $\Delta R < 0.4$ of any jet with $P_T > 25$ GeV and $|\text{JVF}| > 0.75$. Then, a τ candidate is rejected when it is found within $\Delta R < 0.2$ of a selected muon or electron. Next, a jet is removed if found within $\Delta R < 0.2$ of a selected τ object. Finally, jets within $\Delta R < 0.2$ of a selected electron are also rejected.

2.4.6 Missing transverse energy

The missing transverse energy (E_T^{miss}) definition used in this analysis is `MET_RefFinal_em_tightpp`. It is an object-based definition, calculated from topological clusters calibrated at the electromagnetic scale (`EM`) and corrected according to the energy scale of the associated objects. The topological clusters are associated to electrons, high-P_T jets and low-P_T jets. The ordering of these objects indicates the order of association of the clusters to the objects, where the clusters are associated with the first object used. The electron term in E_T^{miss} uses the cluster associated with the electrons from `ElectronAODCollection` that satisfy the `ElectronTight++` definition with $P_T > 10\ GeV$. The electron energy scale used in the E_T^{miss} calculation includes all electron correction factors except the out-of-cluster correction. The jets used for selecting the high- and low-P_T jets come from the `AntiKt4EMJESTopoJets` collection without pile-up corrections. Clusters associated with jets with a $P_T > 20\ GeV$ are corrected at the `EM+JES` scale, while clusters associated with `SoftJets` ($7\ GeV < P_T < 20\ GeV$) are included at the `EM` scale only. The muon term in E_T^{miss} is determined from the P_T of muons from `MuidMuonCollection` for the full acceptance range of the muon spectrometers, i.e. $|\eta| < 2.7$. All combined muons within $|\eta| < 2.5$ are included in E_T^{miss}. The muon term in E_T^{miss} contains both isolated muons (`MET_MU_TRACK`) and non-isolated muons (`MET_MU_SPECTRO`). The remaining energy in the calorimeter not associated with the above objects is included in the E_T^{miss} definition as a `CellOut` term, and calibrated at the `EM` scale.

2.5 Data-driven estimation of backgrounds with misidentified leptons

In order to give a realistic picture of the impact of the multi-jet background on the charged Higgs boson signal, one would have to spend a large amount of computer resources to simulate a sufficiently large dataset of multi-jet events. Indeed, the corresponding production cross section is very large, while the probability that such events pass the final selection cuts is very small. As this is not feasible, methods using the actual data recorded by the ATLAS detector have been applied. Another reason for choosing data-driven methods is that lepton isolation variables are difficult to simulate, since they are sensitive to a detailed modeling of hadronisation and of the detector response.

One of the key features of ATLAS is an excellent lepton identification. This feature is exploited in this analysis, as the trigger and the event selection are both based on the identification of one isolated lepton. However, there is also a non-negligible contribution from non-isolated leptons, arising from the semileptonic decay of a b or c hadron, from the decay-in-flight of a $\pi^{\pm}$ or K meson and, in the case of misidentified electron objects, from the reconstruction of a π^0, photon conversions and shower fluctuations. All leptons coming from such mechanisms are referred to as *misidentified* leptons, as opposed to true isolated leptons (e.g. from the decay of W and Z bosons), which are referred to as *real* leptons.

The fundamental idea of the data-driven method discussed here is to exploit differences in the lepton identification between real and misidentified electrons or muons. For this purpose, two data samples are defined, differing only in the lepton identification criteria, while keeping the same kinematic selections. The first sample contains mostly events with real leptons, and it is referred to as the *tight* sample. The second one contains mostly events with misidentified leptons and is referred to as the *loose* sample. In this analysis, the loose sample is simply obtained by loosening the isolation requirement for the leptons (the tight sample is therefore, by construction, a subset of the loose sample). The selection criteria for the electrons and muons found in the loose samples are discussed in Sections 2.5.1 and 2.5.2.

Let N_r^L and N_f^L (respectively N_r^T and N_f^T) be the numbers of events containing real and misidentifed leptons, which pass the loose (respectively tight) lepton selection. The number of events containing one loose or tight lepton can be written as:

$$N^L = N_f^L + N_r^L, \tag{2.5.1}$$

$$N^T = N_f^T + N_r^T. \tag{2.5.2}$$

Let r and f be the rates for a real or misidentified lepton to be identified as a tight lepton:

$$r = \frac{N_r^T}{N_r^L} \quad \text{and} \quad f = \frac{N_f^T}{N_f^L}. \tag{2.5.3}$$

The number of misidentified leptons passing the tight selection N_f^T can then be re-written as:

$$N_f^T = \frac{f}{r-f}(rN^L - N^T). \tag{2.5.4}$$

The main ingredients of the data-driven method used here to estimate the contribution of the multi-jet background are the efficiencies r and f for, respectively, a true or misidentified lepton to be detected as a real lepton. More details about the computation of these efficiencies will be discussed below. For the method presented here to give reliable and accurate results, any significant dependence of r and f on kinematical or topological observables such as the transverse momentum and pseudorapidity of the lepton, the jet multiplicity, the number of b-tagged jets, etc, must be taken into account and included in the final parameterisation of the efficiencies. In addition, both r and f should be as independent of the sample composition as possible, in such a way that, if r and f are determined in a control region orthogonal to the signal region, they can still be applied in the analysis after the final event selection. Finally, since $r - f$ enters in the denominator of the expression used to compute N_f^T, these efficiencies are required to be numerically different and must therefore be determined in a large control sample, so that the statistical uncertainties are small enough to keep r and f well separated.

2.5.1 Electron selection criteria

While tight electrons are defined exactly as in Section 2.4.3, the loose electrons considered here must pass the following criteria:

- quality requirement `RobustMedium++` with author 1 or 3,
- $E_{\mathrm{T}} > 25$ GeV, where $E_{\mathrm{T}} = E_{clus}/\cosh(\eta_{track})$,
- $|\eta_{clus}| < 2.47$, but not in the transition region $1.37 < |\eta_{clus}| < 1.52$,
- electron isolation requirements with an efficiency of 98% for true electrons.

The measurement of the electron identification efficiency r is derived using a tag-and-probe method with a data sample of $Z \to e^+e^-$ events. Only events consisting of two oppositely charged loose electrons with an invariant mass in the range of 86–96 GeV are taken into consideration. The events are further purified by requiring at least one electron (called "tagged electron") to be tight. The rate at which the other electron (called "probe electron") passes the tight selection criteria defines r_e. On the other hand, a control sample with misidentified electrons is selected by considering data events with exactly one electron passing the loose criteria. In comparison with $W \to e\nu_e$ + jets, these events are characterised by a relatively small missing transverse energy. Hence, to select events dominated by multi-jet production, 5 GeV $< E_T^{miss} < 20$ GeV is required. In such events, the rate at which the loose electron passes the tight selection criteria defines the misidentification rate f_e. It should be noted that the contribution of other SM processes to the control region with 5 GeV $< E_T^{miss} < 20$ GeV is estimated by using Monte Carlo simulations and is subtracted before computing the misidentification rate f_e.

The real and misidentified electron rates (r_e and f_e) are shown in Fig. 2.5.1, as functions of the pseudorapidity of the electron, the distance ΔR between the electron and the nearest jet, the transverse momentum of the leading jet, the number of b-tagged and τ jets, as well as the data-taking period. It should be noted that these measurements are performed on data events passing the single-electron trigger. In addition, this analysis requires the detected electron to be trigger-matched. Hence, the real and misidentified electron rates must be determined with the trigger-matching requirement.

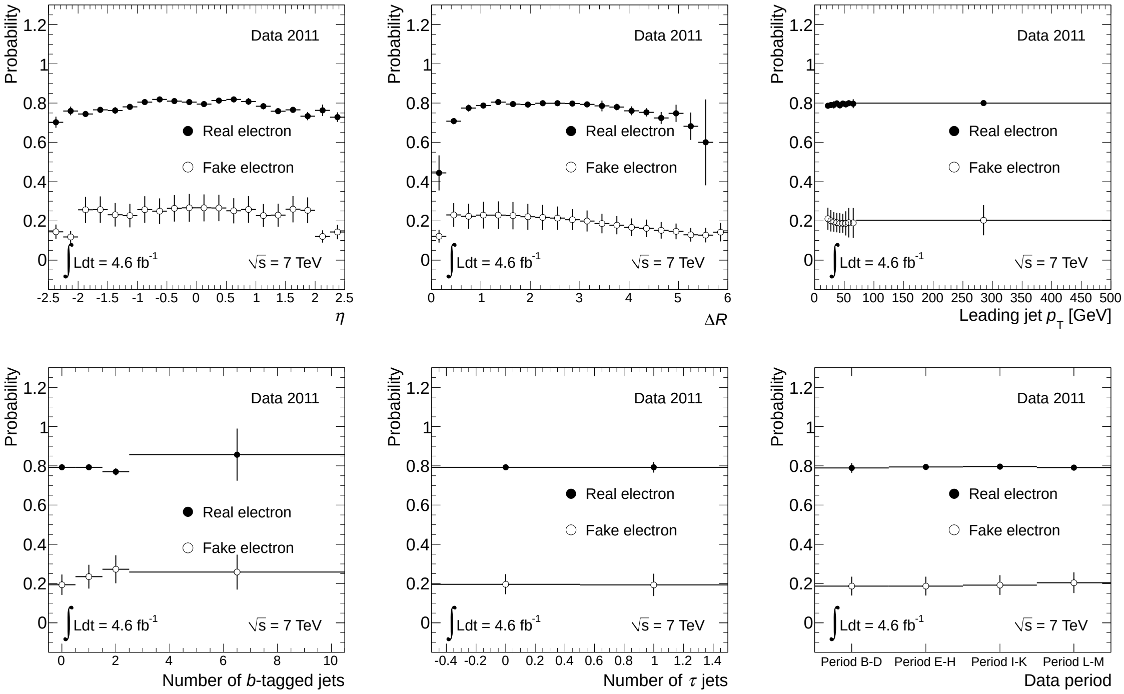

Figure 2.5.1: Real and misidentified electron rates, measured in data, as functions of (from top left to bottom right) the pseudorapidity of the electron, the distance ΔR between the electron and the nearest jet, the transverse momentum of the leading jet, the number of b-tagged and τ jets, and the data-taking period. The rates r_e and f_e are estimated with the trigger-matching requirement.

2.5.2 Muon selection criteria

By definition, loose muons pass all selection criteria listed in Section 2.4.4, except the isolation criteria: `Ptcone30` < 2.5 GeV and `Etcone20` < 4 GeV. In order to measure the real and misidentified muon selection rates (r_μ and f_μ), data events passing the single-muon trigger are considered here. As in the case of electrons, two high-purity control regions for real and misidentified muons are defined.

Events with exactly two oppositely charged loose muons are first selected. The dimuon invariant mass in these events must lie between 86 and 96 GeV. In such a sample enriched with Z boson candidates, one of the muons (called "tagged muon") is further required to pass the tight selection criteria. It is then checked whether the other muon ("probe muon") passes the tight criteria and the corresponding rate is defined as r_μ. The misidentified muon control region is obtained by selecting data events with exactly one loose muon, where 5 GeV $<$ E_T^{miss} $<$ 20 GeV. In such events, the rate at which loose muons pass the tight selection criteria defines the misidentification rate f_μ.

The real and misidentified muon rates (r_μ and f_μ) are shown in Fig. 2.5.2, as functions of the pseudorapidity of the muon, the distance ΔR between the muon and the nearest jet, the transverse momentum of the leading jet, the number of b-tagged and τ jets, as well as the data-taking period. As in the case of electrons, these rates are measured with the trigger-matching requirement.

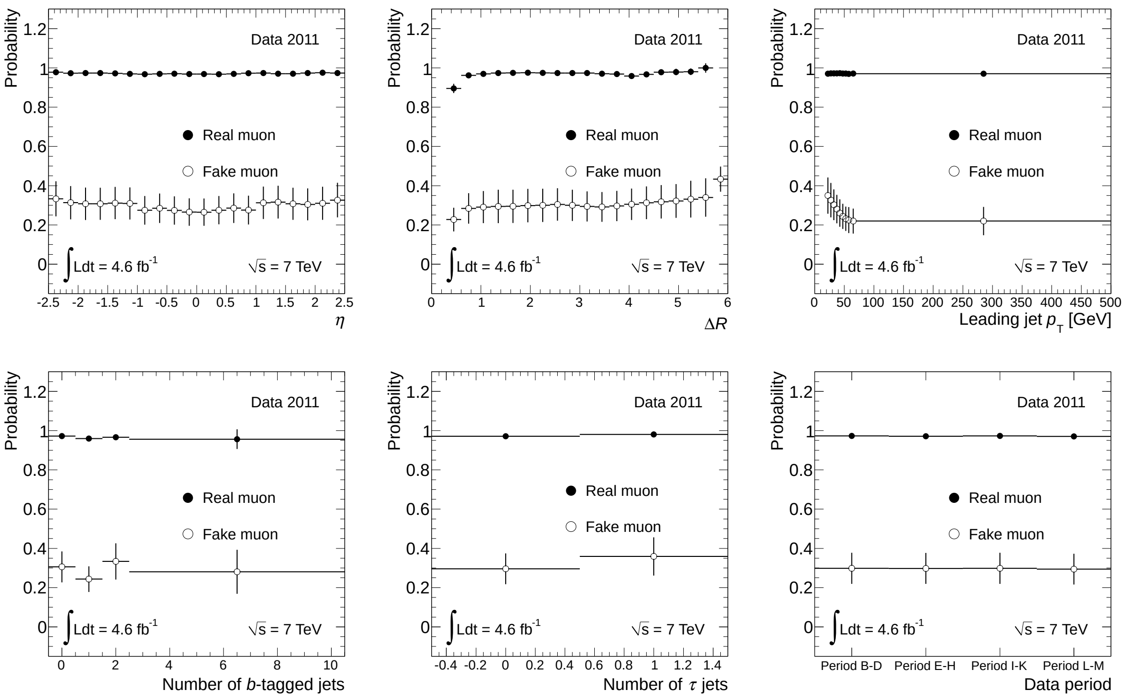

Figure 2.5.2: Real and misidentified muon rates, measured in data, as functions of (from top left to bottom right) the pseudorapidity of the muon, the distance ΔR between the muon and the nearest jet, the transverse momentum of the leading jet, the number of b-tagged and τ jets, and the data-taking period. The rates r_μ and f_μ are estimated with the trigger-matching requirement.

2.5.3 Parametrisation of the real and misidentified lepton rates

In the lepton+jets analysis, f_e and f_μ have a dependence on the pseudorapidity η^l of the lepton, the transverse momentum $p_{\mathrm{T}}(j_1)$ of the leading jet, as well as the distance between the lepton and the nearest jet, Min(ΔR_{lj}). The dependence on the transverse momentum of the leading jet is motivated by the fact that an increase in $p_{\mathrm{T}}(j_1)$ may lead to a higher jet activity in the vicinity of the lepton. In turn, this leads to a reduction of the misidentification rate, as a result of the lepton-jet overlap removal imposed during the object reconstruction. For the same reason, the misidentification rate is expected to decrease for a small Min(ΔR_{lj}), which is likely to occur more often as the jet multiplicity increases. It means that introducing a dependence on Min(ΔR_{lj}) in the parameterisation of the misidentification rate also allows to take into account the slight dependence on the jet multiplicity. Finally, it was found that the shape variations of the real and misidentified lepton efficiencies are negligible from one data-taking period to another. Therefore, data-period dependent variations are only included in the parametrisation of the overall integrated efficiencies.

Hence, if ε denotes both r and f, and if $\langle\varepsilon\rangle$ stands for the average value of ε over the whole sample, the final real and misidentified lepton rates used in this analysis are computed as follows:

$$\varepsilon_{1l} = \varepsilon(\eta^l) \times \frac{\varepsilon(P_T(j_1))}{\langle\varepsilon\rangle} \times \frac{\varepsilon(\text{Min}(\Delta R_{lj}))}{\langle\varepsilon\rangle} \times \frac{\varepsilon(N_b)}{\langle\varepsilon\rangle} \times \frac{\varepsilon(N_\tau)}{\langle\varepsilon\rangle} \times \frac{\varepsilon(\text{data-period})}{\langle\varepsilon\rangle}. \quad (2.5.5)$$

2.6 Study of lepton+jets events

2.6.1 Event selection

The following cuts, optimised using simulation, are applied to select lepton+jets $t\bar{t}$ events for the charged Higgs boson search:

- exactly one lepton, which must furthermore be trigger-matched and have $E_{\mathrm{T}} > 25\,GeV$ (electron) or $P_T > 20\ GeV$ (muon), and exactly zero τ jet;
- at least four jets with $P_T > 20\ GeV$, |JVF| > 0.75 and $|\eta| < 2.4$, including exactly two b-tagged jets (i.e. with a MV1 weight above 0.60);

- to select events with a large E_T^{miss} while rejecting those in which the latter mostly arises from badly reconstructed leptons, i.e. with a small azimuthal angle $\phi_{l,\text{miss}}$ between the lepton and E_T^{miss}:

$$\begin{aligned}
&E_T^{miss} > 40 \text{ GeV} && \text{if } |\phi_{l,\text{miss}}| \geq \pi/6, \\
&E_T^{miss} \times |\sin(\phi_{l,\text{miss}})| > 20 \text{ GeV} && \text{if } |\phi_{l,\text{miss}}| < \pi/6.
\end{aligned}$$

Figure 2.6.1 shows the lepton η distribution, as well as E_T^{miss} after having requested exactly one lepton, zero τ jet and at least two jets (with no requirement on b-tagging). The sum of the Monte Carlo simulated events and of the background with misidentified leptons agrees well with the ATLAS data.

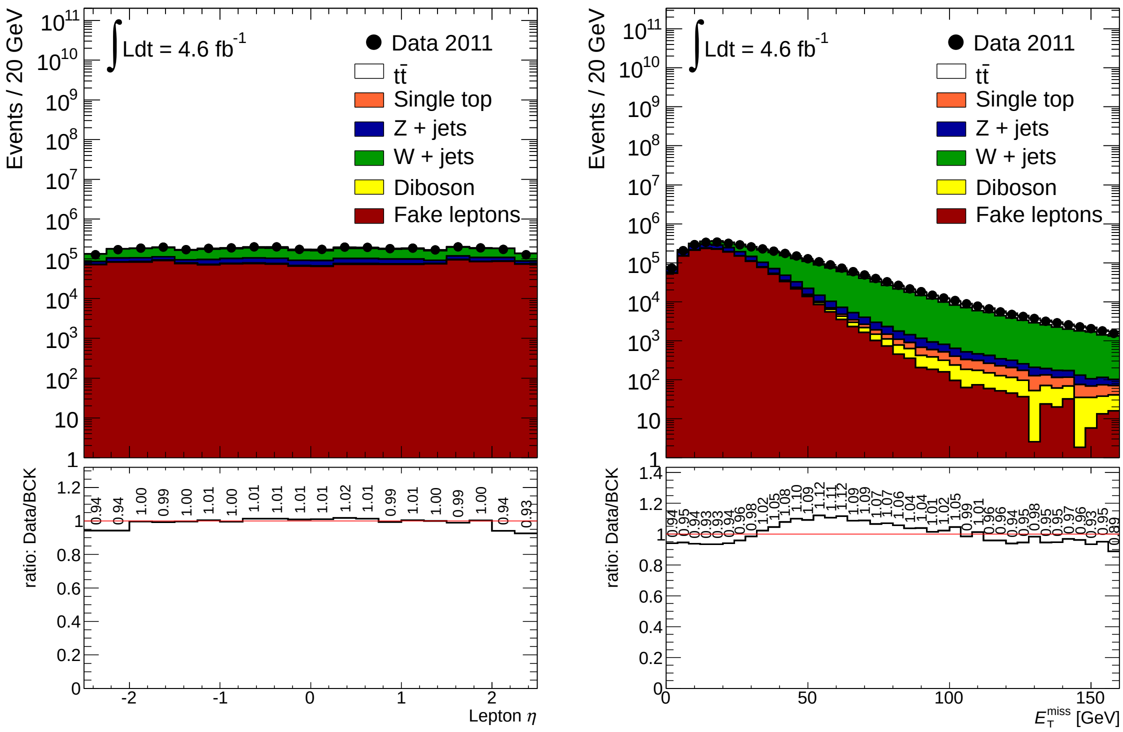

Figure 2.6.1: Lepton η and E_T^{miss} distributions, after having requested exactly one lepton, zero τ jet and at least two jets (with no requirement on b-tagging). The sum of the Monte Carlo simulated events and of the background with misidentified leptons (in red) are compared to the ATLAS data.

Having selected lepton+jets $t\bar{t}$ events, the jets must be correctly assigned. Most of the analysis beyond this point depends on the correctness of this assignment. In particular, the hadronic side of the event is identified by selecting the combination of one b-tagged jet and two untagged jets (j) that minimises:

$$\chi^2 = \frac{(m_{jjb} - m_{\text{top}})^2}{\sigma_{\text{top}}^2} + \frac{(m_{jj} - m_W)^2}{\sigma_W^2}, \tag{2.6.1}$$

where σ_{top} and σ_W are the widths of the reconstructed top quark and W boson, which are estimated from correctly identified combinations in simulated $t\bar{t}$ events, respectively 17 GeV and 10 GeV. In such events, the assignment efficiency is found to be 72%. Having chosen the b-tagged jet associated to the hadronic side, the invariant mass of the top quark candidate is reconstructed, see Fig. 2.6.2. At this stage, all events with $\chi^2 > 5$ are discarded, which in turn selects top quark candidates in the m_{jjb} window 134–211 GeV.

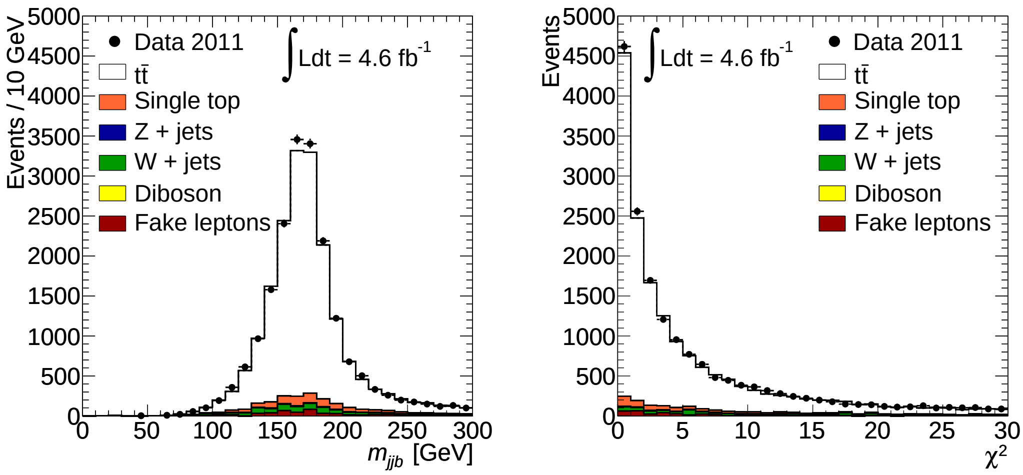

Figure 2.6.2: Reconstruction of the top quark mass and corresponding χ^2 on the hadronic side of the selected lepton+jets events, in ATLAS data and in Monte Carlo simulations (only SM top quark decays $t \to bW$ are considered here, with a cross section of 167 pb).

On the leptonic side of the event, the charged lepton and the missing transverse energy are used to compute the transverse mass m_{T}^W defined in Eq. (2.2.2). Figure 2.6.3 shows the corresponding distribution, in ATLAS data and Monte Carlo simulations. In the presence of a leptonic τ decay, m_{T}^W does not provide any information about the mass of the decaying charged boson, therefore it does not help discriminate between the charged Higgs boson decays and the W indirect tauonic decays. Note that, at this stage, the lepton+jets analysis relies on the theoretical inclusive $t\bar{t}$ production cross section ($\sigma_{t\bar{t}} = 167^{+17}_{-18}$ pb) for the background estimation. Hence, in the presence of a charged Higgs boson in the top quark decays, with a branching fraction $B \equiv \mathcal{B}(t \to bH^+)$, the contributions of SM-like $t\bar{t} \to b\bar{b}W^+W^-$

events to the total background is scaled by $(1 - B)^2$ prior to adding the signal contribution in simulated events.

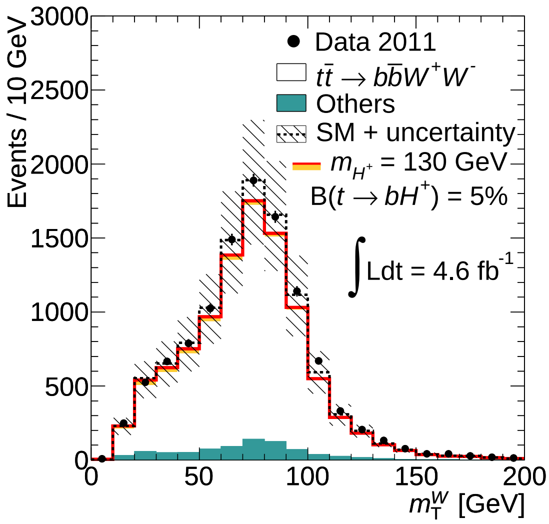

Figure 2.6.3: Distribution of m_{T}^{W} after the lepton+jets event selection, in ATLAS data and in Monte Carlo simulations. The hatched area shows the total uncertainty for the SM background (see Section 2.7.1). The predicted contribution of events with a 130 GeV charged Higgs boson, assuming $\mathcal{B}(t \to bH^+) = 5\%$ and $\mathcal{B}(H^+ \to \tau\nu) = 1$ is also shown.

Table 2.6.1 shows how the event selection affects the SM processes and $t\bar{t}$ events with at least one decay $t \to bH^+$, assuming $m_{H^+} = 130$ GeV and and $\mathcal{B}(t \to bH^+) = 5\%$, which yields a cross section of 16.3 pb for the signal. Events surviving the selection cuts are dominantly lepton+jets $t\bar{t}$ events, as expected.

2.6.2 Reconstruction of the discriminating variables

By using the charged lepton and the b jet associated to the leptonic side of the event, the variable $\cos\theta_l^*$ can be computed. The left-hand plot of Fig. 2.6.4 shows the $\cos\theta_l^*$ distribution obtained in ATLAS data and Monte Carlo simulations.

A control region enriched with $t\bar{t} \to b\bar{b}W^+W^-$ events is defined by requiring $-0.2 < \cos\theta_l^* < 1$. The purpose of this control region is to allow a fit of the product of the cross section σ_{bbWW} for the $t\bar{t} \to b\bar{b}W^+W^-$ process, the branching fraction $\mathcal{B}(t \to bH^+)$, as well as the acceptance and efficiency as one nuisance parameter (with a strong constraint

Sample	Selection cut				
	Trigger & 1 lepton & $N_{jets} \neq 0$	≥ 4 jets	2 b jets	E_T^{miss} cuts	$\chi^2 < 5$
$t\bar{t}$	$1.3 \cdot 10^5$	$7.0 \cdot 10^4$	27986	17513	10058
Single top quark	$4.3 \cdot 10^4$	$6.7 \cdot 10^3$	1890	1141	368
W+jets	$6.6 \cdot 10^6$	$9.2 \cdot 10^4$	1568	866	186
Z+jets	$1.7 \cdot 10^6$	$2.9 \cdot 10^4$	499	96	27
Diboson	$3.6 \cdot 10^4$	$1.6 \cdot 10^3$	45	21	6
Misidentified leptons	$6.9 \cdot 10^6$	$7.4 \cdot 10^4$	3666	502	214
$\sum$ SM	$1.5 \cdot 10^7$	$2.7 \cdot 10^5$	35654	20139	10859
Data	$1.5 \cdot 10^7$	$2.8 \cdot 10^5$	37444	20210	11030
$t \to bH^+$ (130 GeV)	$4.3 \cdot 10^3$	$2.1 \cdot 10^3$	724	483	283
Signal+background	$1.5 \cdot 10^7$	$2.7 \cdot 10^5$	33123	18549	9981

Table 2.6.1: Number of expected events at various stages of the selection, and comparison with 4.6 fb^{-1} of ATLAS data. The last two rows show numbers for a hypothetical H^+ signal with $m_{H^+} = 130$ GeV and $\mathcal{B}(t \to bH^+) = 5\%$.

from the control region) during the limit setting, see Section 2.7.1. In turn, this method ensures that the final results, and in particular the upper limit on $\mathcal{B}(t \to bH^+)$ are kept independent of the theoretical production cross section for $t\bar{t}$. Assuming $\mathcal{B}(t \to bH^+) = 5\%$, the signal contamination in the control region goes from 1.3% for $m_{H^+} = 90$ GeV to 0.4% for $m_{H^+} = 160$ GeV, and therefore remains small.

On the other hand, in order to select a signal region enriched with $t\bar{t} \to b\bar{b}H^\pm W^\mp$ and $t\bar{t} \to b\bar{b}H^+H^-$ events, $\cos\theta_l^* < -0.6$ is required. Also, in order to enhance the decays of charged (W or Higgs) bosons via $\tau \to l\nu_l\nu_\tau$, $m_{\mathrm{T}}^W < 60$ GeV is required. For the events found in this signal region, the transverse mass m_{T}^H is used as a discriminating variable to search for charged Higgs bosons, as illustrated by the right-hand plot of Fig. 2.6.4.

The signal efficiency at the end of event selection, i.e. in the signal region, is determined from Monte Carlo simulations as a function of $m_{H^\pm}$ and results are summarised in

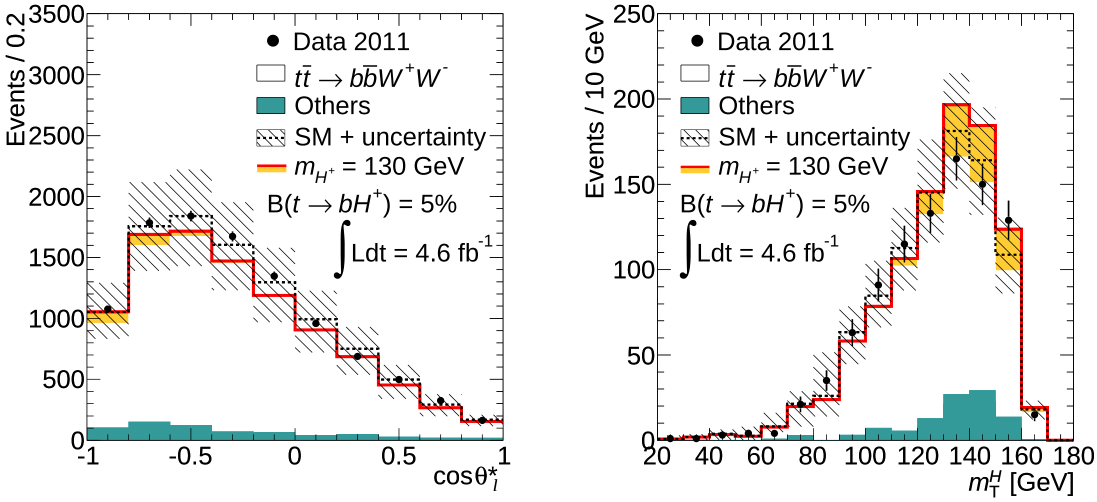

Figure 2.6.4: Distribution of $\cos\theta^*_l$ (left) and of the transverse mass m_T^H (right) when $\cos\theta^*_l < -0.6$ and $m_T^W < 60$ GeV, in ATLAS data and Monte Carlo simulations. The hatched area shows the total uncertainty for the SM background (see Section 2.7.1). The predicted contribution of events with a 130 GeV charged Higgs boson, assuming $\mathcal{B}(t \to bH^+) = 5\%$ and $\mathcal{B}(H^+ \to \tau\nu) = 1$ is also shown.

Table 2.6.2.

H^+ mass [GeV]	Efficiency (%)
90	0.11
100	0.14
110	0.14
120	0.14
130	0.15
140	0.14
150	0.11
160	0.04

Table 2.6.2: Signal efficiency, determined from simulation, as a function of the charged Higgs boson mass.

Table 2.6.3 shows how the event selection affects the SM processes and $t\bar{t}$ events with at least one decay $t \to bH^+$, assuming $m_{H^+} = 130$ GeV and $\mathcal{B}(t \to bH^+) = 5\%$. The ATLAS data are found to agree with the SM expectation and no significant deformation of the m_{T}^{H} distribution is observed.

Sample	Event yield
$t\bar{t}$	$844 \pm 20^{+150}_{-147}$
Single top quark	$28 \pm 2^{+8}_{-6}$
W+jets	$14 \pm 3^{+6}_{-3}$
Z+jets	$2.1 \pm 0.7^{+1.2}_{-0.4}$
Diboson	$0.5 \pm 0.1 \pm 0.2$
Misidentified leptons	$55 \pm 9 \pm 20$
$\sum$ SM	$944 \pm 22^{+151}_{-148}$
Data	933
$t \to bH^+$ (130 GeV)	$125 \pm 4^{+25}_{-27}$
Signal+background	$986 \pm 21^{+139}_{-136}$

Table 2.6.3: Number of expected events in the signal region of the lepton+jets final state, and comparison with 4.6 fb^{-1} of ATLAS data. All electroweak and $t\bar{t}$ backgrounds are estimated from simulation, and an inclusive production cross section of 167 pb is used for $t\bar{t}$. The last two rows show numbers for a hypothetical H^+ signal correspond to $m_{H^+} = 130$ GeV and $\mathcal{B}(t \to bH^+) = 5\%$. Both statistical and systematic uncertainties are shown, in that order.

2.7 Limits on the branching ratio of $t \to bH^+$

Assuming $\mathcal{B}(H^+ \to \tau\nu) = 1$, upper limits are extracted on the branching ratio $B \equiv \mathcal{B}(t \to bH^+)$ as a function of the charged Higgs boson mass. As previously mentioned, the limit setting procedure ensures that the final results are kept independent of the theoretical production cross section for $t\bar{t}$.

2.7.1 Method

Since the signal and the $t\bar{t}$ background are correlated, the event rate of the $t\bar{t} \to b\bar{b}W^+W^-$ background is derived from the measurement in the control region (CR) with $-0.2 < \cos\theta_l^* < 1$, while the signal region (SR) corresponds to $\cos\theta_l^* < -0.6$, with the additional cut on the transverse mass $m_{\mathrm{T}}^W < 60$ GeV.

Let μ_W be the expected number of SM-like $t\bar{t} \to b\bar{b}W^+W^-$ background events and let μ_{others} be the expected background from other SM processes. For any branching fraction B, the expected number of $t\bar{t} \to b\bar{b}H^\pm W^\mp$ events, μ_H, is given by:

$$\mu_H = \mu_W \times \frac{2B}{1-B}. \tag{2.7.1}$$

Note that $t\bar{t} \to b\bar{b}H^+H^-$ events are not considered in the following, as previous studies suggest that top quarks decay into bH^+ in less than 10% of the cases, hence the contribution from $t\bar{t} \to b\bar{b}H^+H^-$ remains very small. By not considering these events, our estimation of the upper limit on $\mathcal{B}(t \to bH^+)$ is somewhat conservative.

We first focus on the control region of the $\cos\theta_l^*$ distribution. If ϵ_W and ϵ_H are the corresponding acceptances of the SM-like $t\bar{t} \to b\bar{b}W^+W^-$ events and of the signal $t\bar{t} \to b\bar{b}H^\pm W^\mp$ events (derived from Monte Carlo simulations), the expected number of events in the control region is:

$$\mu^{\text{CR}} = \mu_W\epsilon_W + \mu_H\epsilon_H + \mu_{\text{others}}^{\text{CR}} = \mu_W\left(\epsilon_W + \frac{2B}{1-B}\epsilon_H\right) + \mu_{\text{others}}^{\text{CR}}. \tag{2.7.2}$$

Let now δ_W and δ_H be scaling factors from the control region to the signal region (also derived from Monte Carlo simulations). The expected number of events in the signal region is:

$$\mu^{\text{SR}} = \mu_W\epsilon_W\delta_W + \mu_H\epsilon_H\delta_H + \mu_{\text{others}}^{\text{SR}} = \mu_W\left(\epsilon_W\delta_W + \frac{2B}{1-B}\epsilon_H\delta_H\right) + \mu_{\text{others}}^{\text{SR}}. \tag{2.7.3}$$

Let m and n be the number of observed events in the control and signal regions, respectively. In the signal region, the simulated transverse mass distribution is described using a probability density function $f_i(m_{\mathrm{T}})$. The expected and observed number of events in each bin i are thus respectively $\mu_i^{\text{SR}} = \mu^{\text{SR}} f_i(m_{\mathrm{T}})$ and n_i. The resulting likelihood is given by:

$$\mathcal{L}(B) = \text{Poisson}(m|\mu^{\text{CR}}) \prod_i \text{Poisson}(n_i|\mu_i^{\text{SR}}) \prod_j p(\tilde{\theta}_j|\theta_j), \tag{2.7.4}$$

where the index i indicates the bin of the discriminating transverse mass variable distribution. Nuisance parameters θ are used to describe the effect of systematic uncertainties, and $p(\tilde{\theta}_j|\theta_j)$ are the Gaussian constraints relating each parameter to its nominal estimate $\tilde{\theta}_j$. We perform a profile likelihood statistical analysis with B as the one parameter of interest and μ_W as an additional nuisance parameter that is only constrained by data in the control and signal regions. The test statistic is given by [74]:

$$q_B = -2\log\frac{\mathcal{L}(B, \hat{\hat{\theta}}_B, \hat{\hat{\mu}}_{W,B})}{\mathcal{L}(\hat{B}, \hat{\theta}, \hat{\mu}_W)}, \quad 0 \leq \hat{B} \leq B, \tag{2.7.5}$$

where $\hat{\hat{\theta}}_B$ and $\hat{\hat{\mu}}_{W,B}$ are the maximum likelihood estimators (MLE) of the nuisance parameters for a fixed B, while $\hat{\theta}$, $\hat{\mu}_W$ and $\hat{B}$ are the global MLEs of θ, μ_W and B, respectively. The limit itself is derived using the CLs criterion [75] based on a fully frequentist ensemble in which n_i, m and $\tilde{\theta}_j$ are randomised.

2.7.2 Systematic uncertainties arising from the object reconstruction

In addition to the uncertainty of 3.9% arising from the measured integrated luminosity, the main detector-related systematic uncertainties are listed in Table 2.7.1. These are mostly related to trigger, reconstruction and identification (ID) efficiencies, as well as the energy/momentum resolution and scale of the objects described in Section 2.4. In order to assess the impact of most sources of systematic uncertainty on the result of the analysis, selection cuts for each analysis are re-applied after shifting a particular parameter by its ± 1 standard deviation uncertainty.

2.7.3 Systematic uncertainties on the background with misidentified leptons

When applying the tag-and-probe method to estimate r, the choice of the window size around the Z mass peak could result in a bias. In order to study its impact, the dilepton invariant mass is chosen in the ranges 84–98 GeV or 88–94 GeV, instead of 86–96 GeV. However, it is found to have only a minor effect (4%). Similarly, the specific choice of the control region in which f is derived might introduce a bias as well. By requiring the missing transverse energy to lie in the ranges 2.5–22.5 GeV or 7.5–17.5 GeV, instead of 5–20 GeV, only

Source of uncertainty	Treatment in analysis
Electron trigger efficiency	Up to 1.0%, depending on P_T, η and the data period.
Electron reco. efficiency	$\pm$ (0.6–1.1)%, depending on η.
Electron ID efficiency	$\pm$ (2.8–3.5)%, depending on E_{T} and η.
Electron energy scale	$\pm$ (0.5–2.4)%, additional constant term, depending on P_T and η.
Electron energy resolution	Up to 1%, depending on E and η.
Muon trigger efficiency	$\pm$ (0.5–6.0)%, depending on η, ϕ and the data period.
Muon reco. efficiency	$\pm$ (0.4–0.8)%, depending on E, η, ϕ.
Muon ID efficiency	$\pm$ (0.3–1.2)%, depending on the data period.
Muon momentum scale and resolution	Up to 1%, depending on P_T, η and the charge.
Jet energy resolution (JER)	$\pm$ (10–30)%, depending on P_T and η.
Jet energy scale (JES)	$\pm$ (2.5–14)%, depending on P_T and η, + pile-up term (2–7%) in quadrature.
Jet reconstruction efficiency	Randomly drop jets (2%) from the events and symmetrise.
b-tagging efficiency	$\pm$ (5–17)%, depending on P_T and η.
b-tagging mistag rate	$\pm$ (12–21)%, depending on P_T and η.
b jet JES uncertainty	Up to 2.5%, depending on P_T, added to the standard JES.
τ ID efficiency	$\pm$ (4–7)%, depending on the number of tracks.
τ energy scale	$\pm$ (2.5–5.0)%, depending on P_T, η and the number of tracks.
E_T^{miss} uncertainty	Uncertainties from object scale and resolution, `CellOut` & `SoftJets` terms + 6.6% flat pile-up contribution.

Table 2.7.1: Main detector-related systematic uncertainties.

a small effect is observed (4–7%). The contamination from true leptons in the control sample used to compute the fake efficiencies is determined, and corrected for, by using Monte Carlo simulated events. It is thus necessary to estimate the effect of the dominant systematic uncertainties (mostly coming from the jet energy scale and resolution) on the backgrounds with fake leptons. These are found to be about 16%. The fake efficiencies are calculated in a control region dominated by gluon-initiated events, but they are later used in a data sample with a higher fraction of quark-initiated events. This sample dependence may introduce a bias on the final background estimation. Therefore, the fake efficiencies are also determined using Monte Carlo simulated events with a different sample composition, namely a QCD sample with a muon filter and a $Zb\bar{b}$ sample. The fake efficiencies computed with these two samples are found to differ by up to 32%. Therefore, a systematic uncertainty is assigned to the backgrounds with fake leptons in order to cover the bias introduced by the sample dependence.

The final systematic uncertainty in the data-driven estimation of the background contribution from events with fake leptons is found to be 36%.

2.7.4 Systematic uncertainties from Monte Carlo generators

To estimate the systematic uncertainty arising from the $t\bar{t}$ generation and the parton shower model, the acceptance for $t\bar{t}$ events is compared between MC@NLO interfaced to HERWIG/JIMMY and POWHEG interfaced to PYTHIA. The relative difference is 6% (8%) in the control (signal) region. The signal is generated with PYTHIA (i.e. at the leading order only), since no other generator is available. In contrast with the SM-like $t\bar{t}$ events, the systematic uncertainty arising from the event generator and the parton shower model is set to the relative difference in acceptance between $t\bar{t}$ events generated with MC@NLO interfaced to HERWIG/JIMMY or with AcerMC (also a leading-order generator) interfaced to PYTHIA. This systematic uncertainty is found to be 7% (10%) in the control (signal) region.

Next, the systematic uncertainty arising from initial and final state radiation is computed by using $t\bar{t}$ samples generated with AcerMC and PYTHIA, where the initial and final state radiation parameters are set to a range of values not excluded by experimental data. Averaging the largest and smallest differences yields a combined systematic uncertainty of 7.2%/10.3% (5.6%/6.1%) in the control (signal) region, for initial/final state radiation.

2.7.5 Results

With the assumption that $\mathcal{B}(H^+ \to \tau\nu) = 1$, Fig. 2.7.1 shows the 95% confidence level (C.L.) upper limits on $\mathcal{B}(t \to bH^+)$ in the lepton+jets channel, see also Table 2.7.2 for numerical values.

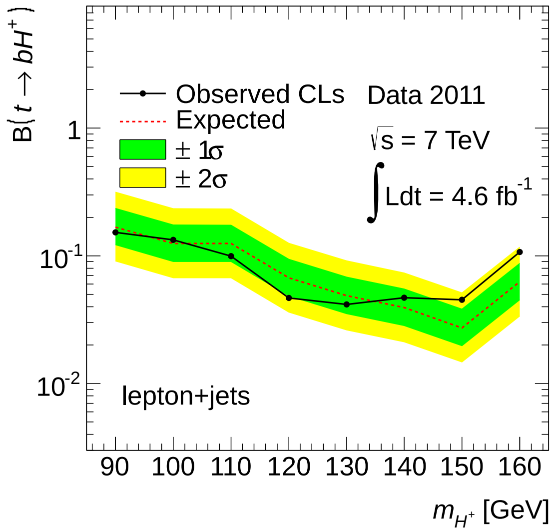

Figure 2.7.1: Upper limits on $\mathcal{B}(t \to bH^+)$ in the lepton+jets channel, as a function of the charged Higgs boson mass, obtained for an integrated luminosity of 4.6 fb^{-1} and with the assumption $\mathcal{B}(H^+ \to \tau\nu) = 1$. All systematic uncertainties are included, as described in the text. The solid line in the figure is used to denote the observed 95% C.L. upper limits, while the dashed line represents the expected exclusion limits. The outer edges of the green and yellow regions show the 1σ and 2σ error bands.

m_{H^+} (GeV)	90	100	110	120	130	140	150	160
95% C.L. observed (expected) limit on $\mathcal{B}(t \to bH^+)$ for the lepton+jets channel	15.2% (16.7%)	13.3% (12.5%)	10.0% (12.5%)	4.7% (6.7%)	4.2% (4.9%)	4.7% (3.9%)	4.5% (2.7%)	10.7% (6.3%)

Table 2.7.2: Observed (expected) 95% C.L. upper limits on $\mathcal{B}(t \to bH^+)$ in the lepton+jets channel, as a function of the charged Higgs boson mass, obtained for an integrated luminosity of 4.6 fb^{-1} and with the assumption that $\mathcal{B}(H^+ \to \tau\nu) = 1$.

In Fig. 2.7.2, the limit on $\mathcal{B}(t \to bH^+) \times \mathcal{B}(H^+ \to \tau\nu)$ is interpreted in the context of the $m_h^{\max}$ scenario of the MSSM [76], in the m_{H^+}-$\tan\beta$ plane. No exclusion limit is shown for charged Higgs boson masses above 140 GeV since that channel is not sensitive enough in that region. The following relative uncertainties on $\mathcal{B}(t \to bH^+)$ are considered and added linearly [77]:

- 5% for one-loop electroweak corrections missing in the calculations,
- 2% for missing two-loop QCD corrections,
- about 1% (depending on $\tan\beta$) for Δ_b-induced uncertainties, where Δ_b is a correction factor to the running b quark mass [78].

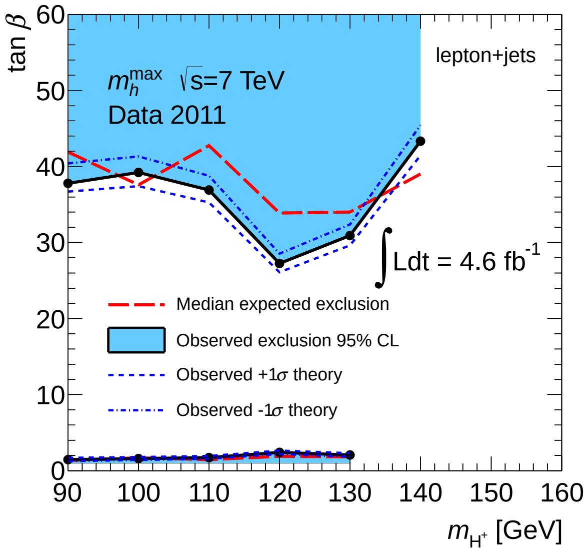

Figure 2.7.2: Limits for charged Higgs boson production from top quark decays in the m_{H^+}-$\tan\beta$ plane, in the context of the $m_h^{\max}$ scenario of the MSSM, obtained for an integrated luminosity of 4.6 fb^{-1}. The 1σ band around the observed limit (blue dashed lines) is obtained by adjusting the theoretical uncertainties listed in the text and adding them linearly.

As one can see, exclusion limits can be obtained also for the low $\tan\beta$ region, since the coupling of the charged Higgs to top and bottom has two competitive parts, $\tan\beta$ and $\frac{1}{\tan\beta}$. This can clearly be seen from the parabola in Fig. 2.7.3. The effect is less than can be expected because, as can be seen in Fig. 2.7.4, the $\mathcal{B}(H^+ \to \tau\nu)$ gets smaller with decreasing $\tan\beta$.

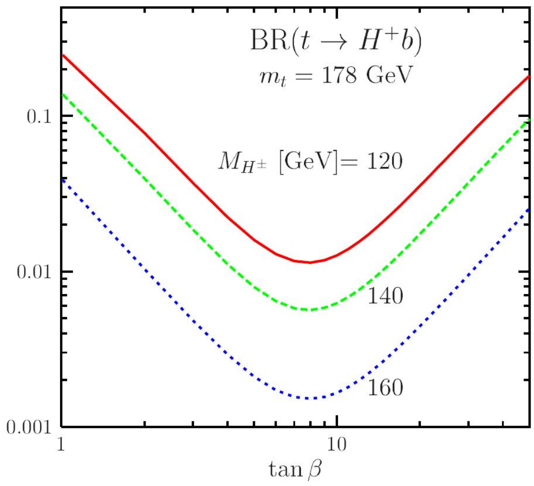

Figure 2.7.3: The branching ratio for the decay $t \to bH^+$ as a function of $\tan\beta$ for several values of m_{H^+} [28]. Note the raise at $\tan\beta < 8$.

2.8 Conclusion

This chapter presents the results of a search for charged Higgs bosons by the ATLAS experiment, based on 4.6 fb^{-1} of proton-proton collision data at $\sqrt{s} = 7$ TeV using the lepton+jets channel in $t\bar{t}$ decays with a leptonically decaying τ in the final state. New discriminating variables were identified in order to distinguish between leptons produced in $\tau \to l\nu_l\nu_\tau$ (e.g. in decays of W or charged Higgs bosons) and leptons arising directly from W boson decays. The data is found to agree well with the SM expectation. Hence, assuming $\mathcal{B}(H^+ \to \tau\nu) = 1$, this leads to upper limits on the branching fraction $\mathcal{B}(t \to bH^+)$ between 4% and 15% for charged Higgs boson masses in the range $90GeV < m_{H^+} < 160GeV$. In the context of the $m_h^{\max}$ scenario of the MSSM, values of $\tan\beta$ larger than 27–44 are excluded in the mass range $90GeV < m_{H^+} < 140GeV$.

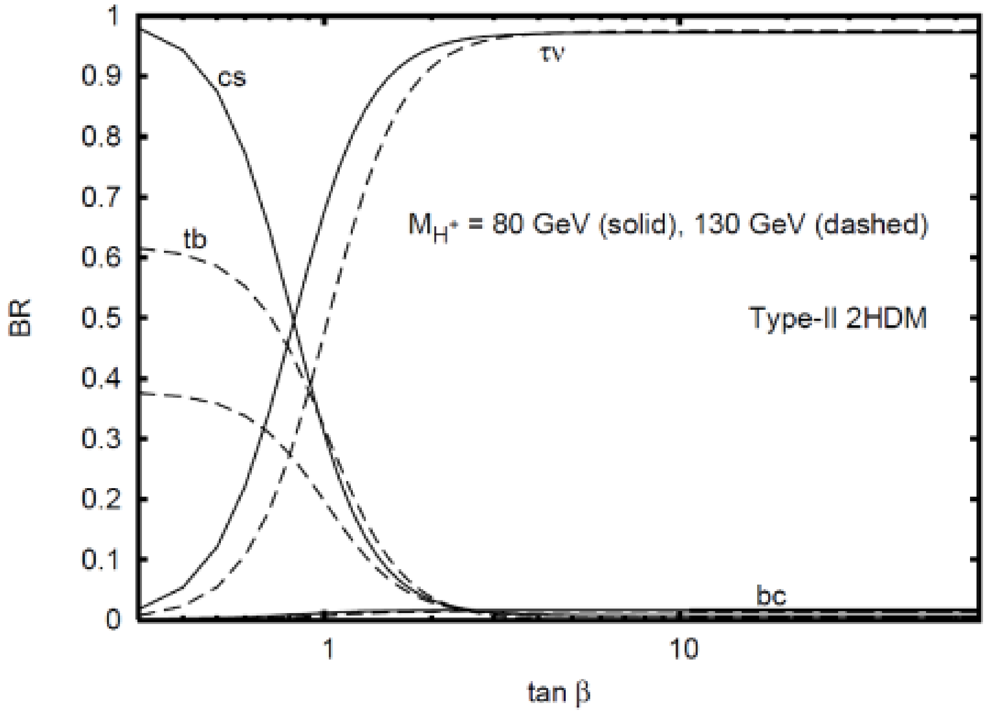

Figure 2.7.4: Charged Higgs branching ratios as a function of $\tan\beta$ for m_{H^+} = 80 GeV (solid lines) and 130 GeV (dashed lines) in the Type-II 2HDMs [79]. Note the dominance of $\tau\nu$ for $\tan\beta > 1$.

3 Standard Model Higgs in High-Luminosity (HL) LHC

The recent discovery of a particle with a mass close to 125 GeV at the LHC, with the properties of a Higgs boson, opens the question of whether this new particle is the Standard-Model (SM) Higgs boson or one physical state of an extended Higgs sector, as predicted in many extensions of the SM, such as 2HDM. One of the ways to answer this exciting question is by measuring precisely the couplings to fermions and determining the spin/CP quantum numbers.

Some of the studies will only be possible in a few years time, once ATLAS will collect more data, hence, they were studied only by using Monte Carlo, projecting into the future. The studies are presented on the prospects of measuring Higgs boson properties in 14 TeV proton-proton collisions at the LHC with 300 fb^{-1} and at the HL-LHC with 3000 fb^{-1}. Generator-level Monte Carlo events are used to perform these studies, with parameterized efficiencies and smearing applied to approximate the expected detector performance under HL-LHC conditions.

All that was used to make a case for the upgrade of the LHC to HL machine (running at 14TeV and collecting integrated luminosity of 3000 fb^{-1}) in the European Strategy symposium.

The chapter is organized in the following way: An introduction is given in Section 3.1. The detector simulations, objects reconstruction and the cross sections for HL-LHC are given in Section 3.2. In Section 3.3 the $VBF, H \to \tau\tau$ channel is described. Section 3.4 presents the $ttH, H \to \mu\mu$ studies. Finally, the coupling fit results are shown in Section 3.5.

My contributions to this study were the $VBF, H \to \tau\tau$ and the $ttH, H \to \mu\mu$. For completeness I show also the final result which are based also on my results (Section 3.5). The analysis was submitted to the European Strategy for Particle Physics, Cracow, Poland, 10-12 September 2012 [7].

3.1 Introduction

The Higgs boson studies documented here are the basis for the Higgs coupling determination results submitted by ATLAS to the briefing book for the European Strategy for Particle Physics [80]. They are also included in the physics case of the ATLAS phase 2 upgrade letter of intent [81]. All studies are based on particle level, applying efficiency and resolution functions to physics objects [82] instead of a full detector simulation. Rather than attempt to study all possible initial and final state channel combinations, the focus is on the main channels that are available today, together with some key rare processes that are sensitive to the otherwise inaccessible t- and μ-coupling. The precision of the cross section times branching ratio measurements (relative to the expected SM ones, i.e. signal strength) is conventionally expressed in terms of the relative uncertainty in the ratio to the Standard Model expectation, $\Delta\mu/\mu$. These signal strength measurements are then interpreted in terms of Higgs boson couplings. The present LHC programme is expected to deliver an integrated luminosity of about 300 fb^{-1} by the year 2022. The peak instantaneous luminosity will be in the range 2 to $3 \times 10^{34} cm^{-2} s^{-1}$. The High-Luminosity LHC upgrade, HL-LHC, would deliver a total luminosity of about 3000 fb^{-1}, at a peak instantaneous luminosity of $5 \times 10^{34} cm^{-2} s^{-1}$. The corresponding average number of pileup events per bunch crossing, which is also conventially denoted by μ, is expected to be about 140, compared to a typical pileup of 50 for the 300 fb^{-1} sample.

3.2 Detectors, Objects and cross sections for HL LHC

In order to approximate the expected detector performance of an upgraded ATLAS detector operating under the HL-LHC conditions, resolution and efficiency "smearing" functions are applied to the generator-level physics objects. In the absence of fully simulated samples with either the upgraded detector design, or these levels of pile-up, the smearing functions were derived from samples using the current ATLAS detector with various values of μ, up to a maximum average of $\mu = 69$ (i.e. 69 pileup events per bunch crossing on the average).

For jets/b-jets, the evolutions of the various parameters as a function of μ at low pile-up were fit with appropriate functions, and then extrapolated up to $\mu = 140$. The P_T thresholds applied keep the rate of fake jets from pileup very low, such that they can be neglected. The

b-tagging light-jet rejection power is decreased by a factor ~ 1.25 in going from $\mu = 0$ to $\mu = 40$, which leads to a factor ~ 2 decrease compared to the $\mu = 0$ case when extrapolated up to $\mu = 140$, according to a negative exponential fit. The energies of the final state particles and jets were smeared with a resolution function based on a P_T and η dependent parametrization. The size of the energy resolution was about 20% for jets depending on P_T and η. In addition, reconstructed objects were randomly rejected to model the expected b-tagging efficiency. The efficiencies are parameterized as a function of P_T and η of the b-jet. The probability of a jet being misidentified as a b-jet is also taken into account when processing background samples. The fake probability is $\approx 1\%$ (jet$\rightarrow$ b-jet) on average and have small P_T dependence.

Non-interacting particles are transformed into a missing transverse energy, E_T^{miss}, quantity by adding an additional component due to resolution effects, depending on the average number of interactions per bunch crossing considered for the event and the $\sum E_T$ of the jets and muons in the event.

All Higgs boson production cross sections are taken from Ref. [83]. The present estimates of the relative scale and (PDF + α_S) uncertainties are shown in Tab. 3.2.1. The uncertainties are listed for the main production modes: gluon-gluon fusion, ggF, vector boson fusion, VBF, and associated production with a W, Z or with top quarks, ttH. Uncertainties in the Higgs boson branching ratios are negligible in comparison. In some cases these theoretical uncertainties begin to dominate the results with 300 or 3000 fb^{-1}.

3.3 $H \rightarrow \tau\tau$

For that channel, only VBF Higgs production is studied (see Fig. 3.3.1), in the modes where both τ leptons decay to an electron or muon and neutrinos (di-lepton) or one τ decays leptonically and the other hadronically. This does not exploit the full potential of $\tau\tau$ final states, as boosted categories and the VH channels also make a significant contribution.

Tau lepton can decay either hadronically (65%) or leptonically (35%). Experimentally, when a tau decays leptonically, meaning to charged lepton and neutrino, its selection goes through the detection of a charged lepton + E_T^{miss}. For leptonically decays of the tau, a single lepton trigger and a E_T^{miss} cut were used. Hadronically decaying taus are reconstructed has

Source of uncertainty	$(\sigma^{+} + \sigma^{-})/2$ (%)
ggF scale	10.3
ggF scale 2-jet	30
ggF scale 2-jet ($\tau\tau \to \ell\tau_{\text{had}}$)	21.5
ggF (PDF + α_S)	6.8
VBF scale	0.55
VBF scale 2-jet	6.0
VBF scale 2-jet ($\tau\tau \to \ell\tau_{\text{had}}$)	2.7
VBF (PDF + α_S)	2.35
WH scale	0.45
WH (PDF + α_S)	3.8
ZH scale	2.25
ZH (PDF + α_S)	3.7
ttH scale	7.6
ttH (PDF + α_S)	8.9

Table 3.2.1: Overview of the relative scale and (PDF + α_S) uncertainties.

taus in the detector. But recognizing the hadronic taus with truth MC is challenging due to the lack of charged hadrons information in the truth MC. Several methods were investigated but didnt succeed to behave as hadronic tau. Finally, the adopted strategy was to:

- search for a tau particle (abs(pdgId)==15),
- remove taus decaying to a lepton (electron, muon or tau) to classify the remaining taus (65%) as hadronic taus.

Although these taus are a bit more energetic than the visible hadronic tau (the visible part of the taus after removing the neutrino 4 vector), they had the best performance. In addition, no information was saved regarding the number of tracks in the tau decay. A random number to thus decide the used performance was tossed over a uniform distribution of 77% for 1 track and 23% for 3 tracks.

The VBF special topology (two additional forward jets in the event) is used to identified the candidate events. But in high pileup region, one can find more problems with fake jets from pileup. Dealing with that is hard when using only truth information and so in order to estimate fake jets from pileup, fake jets were added randomly to the events (η dependence) with P_T higher than the equivalent P_T for 10% fake. The fake rate was measured to be less than 5% at the end of the cut flow (0% after the mass cut).

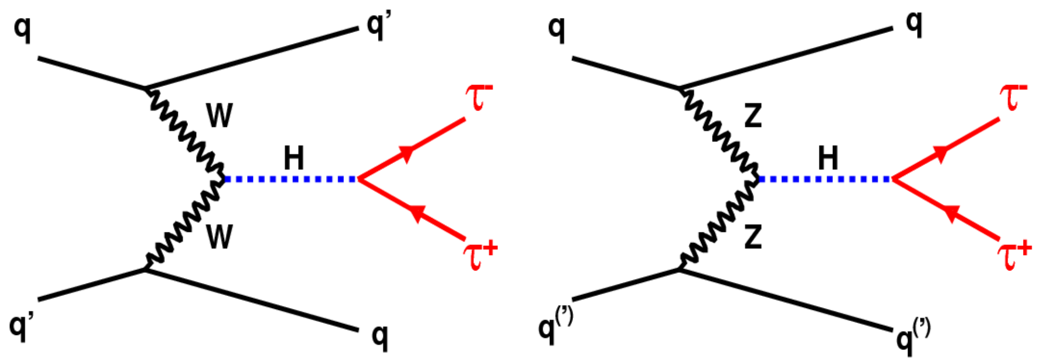

Figure 3.3.1: Example of a leading-order Feynman diagram for the VBF production of $H \rightarrow \tau\tau$.

3.3.1 VBF $H \to \tau\tau \to \ell^+\ell^- 4\nu$

The di-lepton final state is studied first. Although the lepton-hadron final state has a higher branching ratio, the τ identification is more difficult specially at truth level.

3.3.2 Cross check with 7 TeV samples

In order to make sure that using smearing generator level objects with the parameterised performance is a valid assumption, some basic verifications are performed. Agreement in the numbers of events selected using smeared and full simulation is found at the level of 2%. A scale factor of 1.02 is therefore used to scale the 14 TeV smeared results. Compared to the published analysis [84], an aditional cut is included here on the mass of the Higgs candidate, $m_{\tau\tau} > 110\,\mathrm{GeV}$, based on the separation of the signal and the main background, $Z \to \tau\tau$. The mass is calculated in the collinear approximation, where the neutrinos from the τ decay are assumed to be aligned with the visible decay products.

For the 5 fb^{-1} 7 TeV sample, after all cuts except the new mass cut, there are 0.96 signal events and 18.4 background events. The S/B is 0.052. After the mass cut, there are 0.72 signal events and 3.95 background events (S/B = 0.18).

3.3.3 14 TeV analysis at 300 & 3000 fb^{-1}

The signal and main backgrounds at 14 TeV are estimated for 300 and 3000 fb^{-1}. The following selection cuts are applied:

- lepton P_T cut - 25/35 GeV (300/3000 fb^{-1});
- tagged jet P_T cut giving fake rate = 1% / 0.5% for 1st/2nd highest jet;
- central jet veto P_T cut giving fake rate = 10%;
- for the E_T^{miss} smearing, average pileup rates of $\mu = 10/150$ are assumed for 300/3000 fb^{-1}.

In moving from 7 TeV to 14 TeV, the efficiencies of the cuts are compared between the two centre-of-mass energies for the 300 and 3000 fb^{-1} scenarios. The agreement is very good, although the E_T^{miss} modelling is not exact, which influences the collinear approximation cut. It was also verified that the $m_{\tau\tau}$ cut is still appropriate.

After all cuts, the expected number of signal events is 55.9 / 147.2 for 300/3000 fb^{-1} with 56.2 / 189.7 background events. This can be seen for 300 and 3000 fb^{-1} in Table 3.3.1.

	300 fb^{-1}		3000 fb^{-1}	
Cuts	Signal	$Z \to \tau\tau$	Signal	$Z \to \tau\tau$
2 opposite sign leptons	1271	344095	9468	2043376
$30GeV < m_{ll} < 75/100GeV$	1112	314938	8045	1833202
At least 1 jet	838	208180	6225	1346453
$E_T^{miss} > 40/20GeV$	730	140732	5947	1270912
$0.1 < x_1, x_2 < 1.0$	571	14967	2077	379406
$0.5 < \Delta\Phi_{ll} < 2.5$	490	97887	1829	335610
at least 2 jets	180	38064	683	134733
$\Delta\eta_{jj} > 3.0$	79	541	280	1674
$m_{jj} > 350$	79	541	280	1674
b jet veto	78	541	278	1674
Central jet veto	70	381	250	869
$m_{\tau\tau}$	54.8	55.2	144	186

Table 3.3.1: Cut flow table for the $H \to \tau\tau \to \ell^+\ell^-4\nu$ signal and main background for 14 TeV assuming 300 and 3000 fb^{-1}

3.3.4 VBF $H \to \tau\tau \to \ell\tau_{had}3\nu$

Although the mixed leptonic-hadronic decay channel has a higher branching ratio than the di-lepton channel, it is very challenging. Improvements in the hadronic τ identification and Higgs mass estimation which were made between Spring and Summer 2012 are not included for the 14 TeV studies here, and the collinear approximation is used, as for the di-lepton analysis.

The cut flow of the results at 7 TeV derived from generator level has been compared with the official Moriond 2012 results (based on full simulation) to validate the methods and assumptions. Some differences are found in the τ identification, E_T^{miss} and mass calculation.

In moving from 7 TeV to 14 TeV, the relative efficiencies of the cuts between the 7 TeV and the 14 TeV for the 300 and 3000 fb^{-1} scenarios have been compared. All efficiencies stay practically the same apart from the cut on at least two jets, which drops by a factor two from 7 TeV to 14 TeV and the cut on the transverse mass where the efficiency drops by a factor three from 300 fb^{-1} to 3000 fb^{-1} due to the larger pile-up.

The comparison of the S/B for the two 14 TeV luminosity scenarios is given in Table 3.3.2. The $m_{\tau\tau}$ distributions are shown in Fig. 3.3.2. Again, due to lack of statistics in simulating $Z \rightarrow \tau\tau$ events at 14 TeV, the shape of the 7 TeV was used, normalised to the 14 TeV (3000 fb^{-1}) expectations.

	Signal 14 TeV 300 fb^{-1}	Signal 14 TeV 3000 fb^{-1}
Signal	144.7	297.1
Background	628.1	1604.8
S/B	0.23	0.19

Table 3.3.2: Comparison of the S/B for $H \rightarrow \tau\tau \rightarrow \ell\tau_{had}3\nu$ for 300 fb^{-1} and 3000 fb^{-1} at 14 TeV.

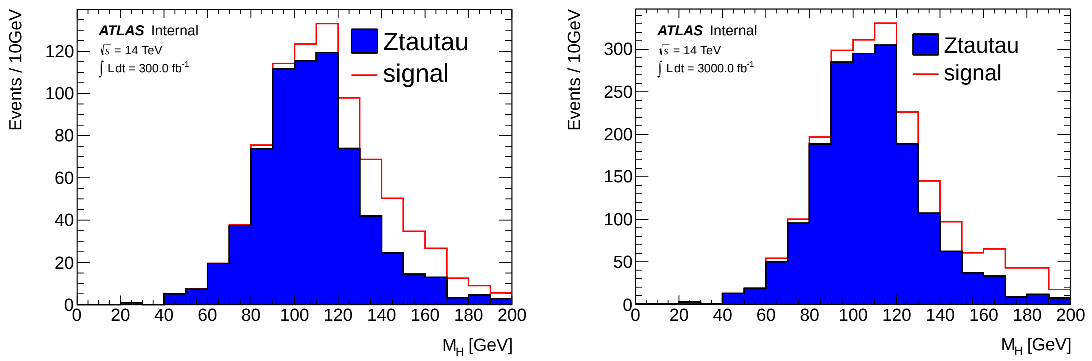

Figure 3.3.2: m_H for the $H \rightarrow \tau\tau \rightarrow \ell\tau_{had}3\nu$ signal and $Z \rightarrow \tau\tau$ at 14 TeV for 300 fb^{-1} and 3000 fb^{-1}.

3.3.5 Extrapolation of current $\tau\tau$ results to 300 fb^{-1}

For the $\tau\tau$ channels, a combination of dedicated analysis targeted at all available initial and final states is needed to reach the best sensitivity. This is illustrated by scaling the expected sensitivity at 7 and 8 TeV with $\sim$10 fb^{-1} to 14 TeV and 300 fb^{-1}. From the scaling of all $\tau\tau$ channels one expects roughly twice as precise a measurement as from the VBF channels alone. A similar improvement is also expected at 3000 fb^{-1}; however a better quantification is currently not possible.

Going from 8 TeV to 14 TeV, the signal Higgs cross-section for a boson mass of 125 GeV increases by a factor 2.6, and the Drell-Yan $Z \rightarrow \tau\tau$ background increases by a factor 1.8. This means that $S/\sqrt{B}$ increases by a factor of 1.9. However, because of more severe pileup conditions at the higher instantaneous luminosity, the analysis may have to be adjusted and this factor of 1.9 may not be achievable. So, assuming the sensitivity from the present analysis, an extrapolation to 300 fb^{-1} at $\sqrt{s} = 14\,\text{TeV}$ gives a signal significance of 6.9 σ, i.e. a 14.5$\%$ error on the signal strength. The contributions due to theory uncertainties are 8.9$\%$, and subtracting these in quadrature gives an estimated uncertainty of 11.4$\%$ without theory errors.

3.4 $H \rightarrow \mu\mu$

The sensitivity of ATLAS to the rare process $H \rightarrow \mu\mu$ is studied for the benchmark mass point of $m_H = 125 GeV$. This channel allows the coupling to second generation fermions to be probed, and can contribute to mass measurements due to the high resolution of the reconstructed $\mu\mu$ invariant mass. Searches in this channel are challenged by the low branching fraction of the $H \rightarrow \mu\mu$ decay. The analysis also uses smeared generator-level samples.

3.4.1 ttH, $H \rightarrow \mu\mu$

A study of this rare channel (see Fig. 3.4.1) has two motivations. First, it allows a direct measurement of the product of the top- and the μ-Yukawa coupling, which are both not accessible through the standard Higgs channels. Second, this channel could be valuable for the determination of the CP nature of the resonance at 125 GeV. Having a vector boson coupling

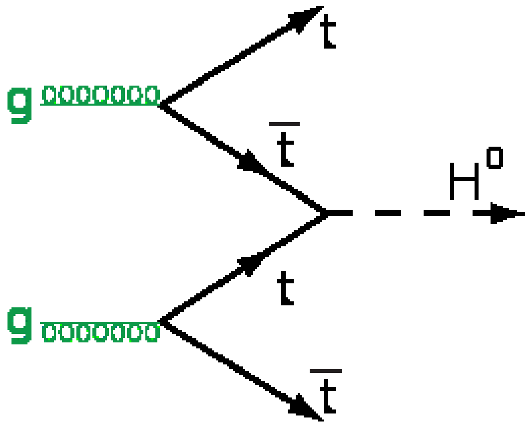

Figure 3.4.1: Example of a leading-order Feynman diagram for the ttH production of $H \to \mu\mu$.

in either the initial or final state is most likely projecting only to the CP even component of the Higgs. For ttH, $H \to \mu\mu$ fermion Yukawa couplings appear both in the initial and final states. Hence no CP suppression is expected. Alternatively also bb or $\tau\tau$ final states could have been used, however these suffer to a far larger extent from reconstruction problems at high luminosities.

The obvious drawback of this channel is that at 14 TeV the ttH cross section is 0.61 pb and the branching ratio $H \to \mu\mu$ is still only $2.2 \cdot 10^{-4}$. Also, having to reconstruct 2 top quarks might be problematic and usually the semi leptonic channel is favoured, but then there is an additional suppression by a factor of 0.325. One solution might be to reconstruct only one top. The hadronic top will be preferred since it has higher branching fraction and can be fully reconstructed.

The method is to follow the a1, a2, b1-b4 variable definitions as in Ref. [85] to determine the CP. The signal samples of the CP even (H) and CP odd (A) were generated using Madgraph5 showered with Pythia 8.

The events must satisfy the following:

- at least two muons with 35GeV,
- no more than four leptons,
- the two muons have opposite charge,

- at least 4 jets (including the b-jet),
- and the mass of the Higgs candidate, formed from the two muons, is between 120 and 130 GeV.

The efficiencies of these cuts on the 14 TeV samples with 3000 fb^{-1} are listed in Table 3.4.1. Finally, the distribution of the di-muon mass is shown in Fig. 3.4.2.

Cuts	$ttH \to \mu\mu$	$ttA \to \mu\mu$	ttZ
At least 2 μ	59	61	1.5
Opposite Sign	89	90	90
At least 4 jets	33	36	19
$120 < M_H < 130 GeV$	82	79	1.5

Table 3.4.1: Comparison of the efficiency for the ttH, $H \to \mu\mu$ channel for the ttH, ttA and ttZ samples at 14 TeV.

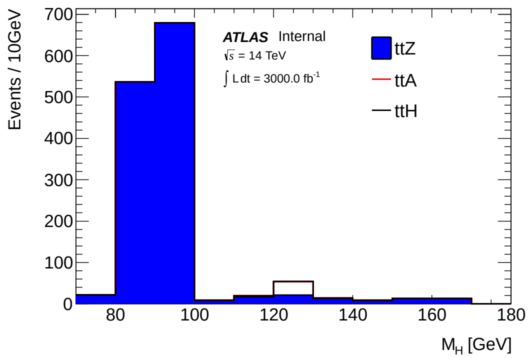

Figure 3.4.2: The invariant mass of the di-muon system in the ttH, $H \to \mu\mu$ channel.

The expected number of events after all the selections is 33 (22) for signal (background). In order to select only tt events few more cuts were tried such as $\chi^2 < 10$ and at least one b jet, yielding results of 12 (9) signal (background) events, but no improvement was observed as statistics is then too limited.

3.4.2 Studies of the parity

By the end of 2012, both ATLAS and CMS have collected a total of about $5\,\mathrm{fb}^{-1}$ and $23\,\mathrm{fb}^{-1}$ of pp collisions at $\sqrt{s} = 7$ TeV and 8 TeV respectively. This dataset allows the first measurements of the spin and parity of the new particle. The observation of CP-violation in the Higgs sector will, however, require significantly larger amounts of data. The analysis has been discussed in section 3.4.1. In addition to the cross section also the angular variables defined in [85] have been analysed. Although the a1 and a2 variables are the most sensitive, the number of expected events for 3000 fb^{-1} is not sufficient for a significant discrimination beyond the $\sim 1\sigma$ level, assuming a SM Higgs signal rate.

3.5 Coupling fit

The combination of Higgs channels for a coupling properties determination is done in the same way as for Ref. [86]. This section is presented to show the results of my analysis ($H \rightarrow \tau\tau$ and the $H \rightarrow \mu\mu$) in the context of the global coupling fit. My results are summarized in tables 3.5.1 - 3.5.3. The final global couplings fit is shown in Fig. 3.5.1.

My own contribution is the $VBF, H \rightarrow \tau\tau$ and the $ttH, H \rightarrow \mu\mu$.

Channel	Sub-channel	Background	ggF	VBF	WH	ZH	ttH
$H \to \tau\tau$	$ll4\nu$	$56^{\pm 7.5}_{\pm 4.7}$	$14^{\pm 3.7}_{\pm 4.4}$	$60^{\pm 7.5}_{\pm 7.5}$	0	0	0
	$l\tau_{\text{had}}3\nu$	$630^{\pm 25}_{\pm 75}$	$40^{\pm 6.0}_{\pm 9.0}$	$140^{\pm 12}_{\pm 22}$	0	0	0
$H \to \mu\mu$	ttH, H	$2^{\pm 1.5}_{\pm 0.043}$	0	0	0	0	$3^{\pm 1.8}_{\pm 0.40}$

Table 3.5.1: Overview of the different Higgs channels used for the coupling fit and the expected events $N^{\pm\text{stat}}_{\pm\text{syst}}$ at 14 TeV, 300 fb^{-1}.

Channel	Sub-channel	Background	ggF	VBF	WH	ZH	ttH
$H \to \tau\tau$	$ll4\nu$	$190^{\pm 14}_{\pm 14}$	$40^{\pm 6.1}_{\pm 12}$	$150^{\pm 12}_{\pm 20}$	0	0	0
	$l\tau_{\text{had}}3\nu$	$1600^{\pm 40}_{\pm 180}$	$70^{\pm 8.6}_{\pm 24}$	$300^{\pm 17}_{\pm 48}$	0	0	0
$H \to \mu\mu$	ttH, H	$22^{\pm 4.6}_{\pm 0.43}$	0	0	0	0	$33^{\pm 5.7}_{\pm 4.0}$

Table 3.5.2: Overview of the different Higgs channels used for the coupling fit and the expected events $N^{\pm\text{stat}}_{\pm\text{syst}}$ at 14 TeV, 3000 fb^{-1}.

	300 fb^{-1}		3000 fb^{-1}	
	w/theory	wo/theory	w/theory	wo/theory
$H \to \mu\mu$	0.525	0.505	0.207	0.164
$ttH, H \to \mu\mu$	0.733	0.719	0.260	0.230
$VBF, H \to \tau\tau$	0.227	0.189	0.202	0.160
$VBF, H \to \tau\tau$ (extrap)	0.146	0.114		

Table 3.5.3: Relative uncertainty on the signal strength for the combination of Higgs analysis and coupling properties fits at 14 TeV, 300 fb^{-1} and 3000 fb^{-1}, assuming a SM Higgs Boson with a mass of 125 GeV. The numbers that changed since the European Strategy submission are highlighted in red.

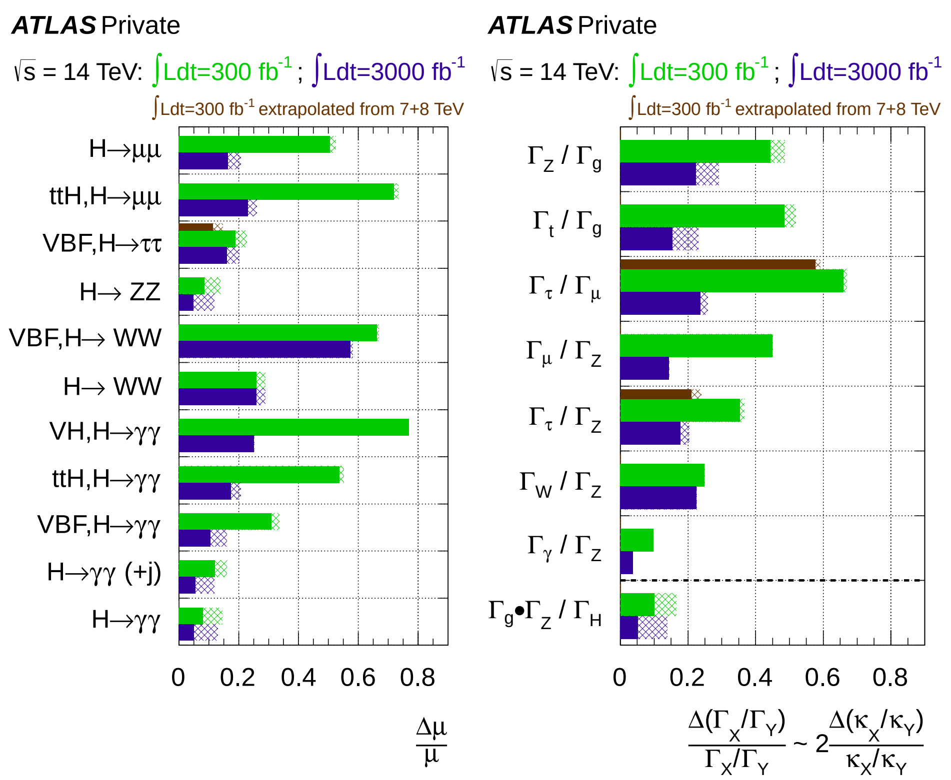

Figure 3.5.1: Combination of Higgs analysis and coupling properties fits at 14 TeV, 300 fb^{-1} and 3000 fb^{-1}, assuming a SM Higgs Boson with a mass of 125 GeV. Left: uncertainty on the signal strength, combining a few channels. Right: uncertainty on ratios of partial decay width fitted to all channels. The hashed areas indicate the increase of the estimated error due to current theory systematics uncertainties.

My own contribution is the $VBF, H \to \tau\tau$ and the $ttH, H \to \mu\mu$.

4 BSM Higgs boson searches at a High-Luminosity LHC

The ATLAS experiment at the LHC is in an excellent position to study possible extensions of the Higgs sector of the Standard Model. This chapter reports results on the expected sensitivity to some beyond-the-Standard-Model physics scenarios with 300 and 3000 fb^{-1} of pp data at $\sqrt{\mathrm{s}} = 14$ TeV. The scenario of a gluon-fusion produced narrow CP-odd particle, A, which decays to $Zh \to \ell\ell bb$, where h is the Standard-Model-like Higgs boson, $\ell = e, \mu$, is motivated by two-Higgs-doublet models.

The chapter is organized in the following way: An introduction and theoretical background is given in Section 4.1. In Section 4.2 the $A \to Zh \to \ell\ell bb$ analysis is described. The results are given in Section 4.3 and the conclusions in Section 4.4.

The analysis of this channel was done in collaboration with a colleague, Allison McCarn except for the concluding statistical analysis which is shown for completeness. The analysis was submitted to the ECFA High Luminosity LHC Experiments Workshop, Aix-les-Bains, France, 1-3 October 2013 [8].

4.1 Introduction and Theoretical Background

The ATLAS and CMS collaborations announced the discovery of a Higgs-like boson in the summer of 2012 [1,2] and since then significant progress has been made in understanding its properties [87, 88]. One question that emerges naturally now is whether the Higgs sector is minimal, i.e. including only one complex doublet of fields, or extended. This question will be certainly an important part of the physics programmes of the LHC upgrade. In this chapter an ATLAS sensitivity study of processes motivated by extended Higgs sectors is presented, for integrated luminosities of 300 and 3000 fb^{-1} at $\sqrt{\mathrm{s}} = 14$ TeV.

The sensitivity to a 2HDM-inspired signature is studied here, in which a CP-odd particle A is produced via gluon-fusion. The decay mode considered is $A \to Zh$, $Z \to ee/\mu\mu$, $h \to b\bar{b}$, where h is the 125 GeV Standard Model (SM)-like Higgs boson. The details of this study are described in Section 4.2. The results are then showed in Section 4.3. Finally, Section 4.4 is devoted to the conclusions.

The production of a heavy CP-odd particle A, which is part of the 2HDM scalar sector, proceeds mainly through gluon-fusion or in association with b-quarks. Gluon-fusion cross sections are calculated using `SusHi 1.1.0` [89] with up to NNLO QCD corrections. The gluon-fusion cross section for type-I 2HDMs is shown in Fig. 4.1.1 left as a function of m_A for $\tan\beta = 1$ and 10, $\sin(\beta - \alpha) = 0.99$ and $m_h = 125$ GeV. In type-I 2HDMs the b-associated production cross section is very small and amounts to less than 0.3% of the gluon-fusion cross section for the parameter space that is studied here. On the contrary, in type-II 2HDMs b-associated production can dominate at large $\tan\beta$. The ratio of b-associated production with respect to gluon-fusion is $< 4\%$ for $\tan\beta = 2$ and up to $\sim 25\%$ for $\tan\beta = 3$ for the parameter space that is studied here. Since only A production from gluon-fusion is considered in this note, no exclusion plots are shown for type-II 2HDMs with $\tan\beta > 3$.

The decay of the A boson may occur in a variety of channels depending on couplings and phase space. Decays to fermions like $A \to \tau\tau/\mu\mu$ have been already studied in the context of MSSM Higgs searches [90–92]. In the framework of the MSSM, these searches exclude the full region $\tan\beta > 5$ for $m_A < 300$ GeV, but for higher m_A their sensitivity decreases. In more general 2HDMs, many decays involving a boson in the final state become available, e.g. $A \to Zh, ZH, WH^{\pm}$, depending also on the masses of the other Higgs bosons. In the study described in Section 4.2, the $A \to Zh$ decay has been chosen, due to the simplicity of the final state. The AZh vertex factor in 2HDMs is type-independent and proportional to $\cos(\beta - \alpha)$. This channel is, in general, the dominant decay mode of A in any 2HDM when m_A is above the Zh kinematic threshold $m_h + m_Z$ and below $2m_{\rm top}$ and it is more relevant at low $\tan\beta$. The branching ratios BR($A \to Zh$) are calculated with `2HDMC 1.41` [93]. An example of the BR($A \to Zh$) for type-I 2HDMs, $\sin(\beta - \alpha) = 0.99$ and $\tan\beta = 1$ is shown as a function of m_A in Fig. 4.1.1 right. For this calculation, as well as for all 2HDM interpretations of the results of this study, $m_A = m_H = m_{H^{\pm}}$ and $m_h = 125$ GeV are assumed.

The $A \to Zh$ search results are interpreted in type-I and type-II 2HDMs, where the potential parameter that softly breaks the $\mathcal{Z}_2$ symmetry is chosen to be $m_{12}^2 = m_A^2 \tan\beta/(1+\tan^2\beta)$. The study focuses on the SM-like limit of the 2HDM and hence values of $\sin(\beta-\alpha)$ close to unity are selected.

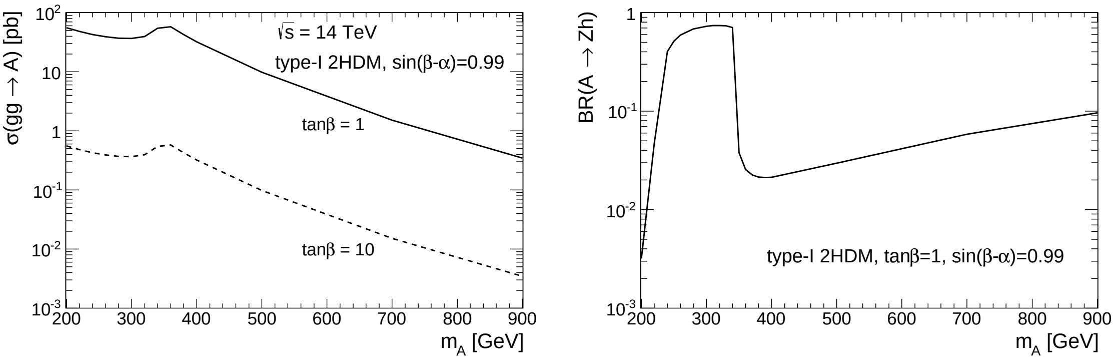

(a) (b)

Figure 4.1.1: The gluon-fusion production cross section (a) and the branching ratio BR($A \to Zh$) (b) for a CP-odd Higgs boson A as a function of its mass, m_A, for $\sin(\beta - \alpha) = 0.99$ and type-I 2HDMs. More details on the assumptions and the calculation are given in the text.

4.2 Analysis of $A \to Zh$ with $Z \to ll$ and $h \to b\bar{b}$

The decay channel $A \to Zh \to llbb$ (with $l = e$, μ) provides a clean signature and a fully reconstructible A boson mass. Signal samples are generated using `Madgraph5 1.5.11` [94] for masses of the A boson spanning the range from 220 GeV to 900 GeV. A narrow A boson width, much smaller than the experimental resolution, is assumed. Parton showering is performed with `Pythia 8.1` [95]. A major SM background process for this final state is Z production in association with light and heavy flavour jets. Events for these processes are generated with `Alpgen` [96] with up to 5 partons in the final state for Z produced in association with light flavour quarks or gluons and up to 2 partons in the final state for Zbb production. The production of $t\bar{t}$ pair events is done with `MC@NLO` [43]. Parton showering and hadronization for both Z+jets and $t\bar{t}$ events is performed with `Herwig 6` [46]. Di-boson events containing two Z bosons are produced with `Pythia 8.1` and the same generator is used for parton showering and hadronization. The theoretical cross sections at NNLO are used for Z+jets backgrounds [97], the approximate NNLO is used for $t\bar{t}$ [49], and the cross section for ZZ is obtained at NLO from `MCFM` [98]. ATLAS searches for the SM $Zh \to llbb$ channel [99] have shown that the multi-jet background is negligible after the full selection cuts, hence this background is not considered here.

Outgoing truth-level (i.e. from the Monte Carlo generator event record) electrons, photons and hadrons are clustered into anti-k_T jets with radius parameter R = 0.4 [68]. Samples using detailed GEANT4-based [64] simulations of the ATLAS detector [65] under the high pile-up conditions expected in the LHC upgrade phases have been analysed to estimate the selection efficiency and resolution of physics objects. The results of these studies have been used to smear the particle-level output after parton showering and hadronization [82]. The study presented here has assumed an average number of interactions per bunch crossing of 140.

Objects that are used in this study are required to pass the following criteria[7] :

- Electrons: $E_T > 25$ GeV, $|\eta| < 2.47$, excluding the region $1.37 < |\eta| < 1.52$, this cut has a 43% (55%) efficiency for the signal with m_A of 360 (700) GeV.
- Muons: $p_T > 25$ GeV, $|\eta| < 2.5$, this cut has a 56% (65%) efficiency for the signal with m_A of 360 (700) GeV.
- Jets: $|\eta| < 2.5$ and p_T cut such that the fake rate due to pile-up jets is less than 1% (41 GeV for $|\eta| < 2.1$, 77 GeV for $2.1 < |\eta| < 2.5$). This cut has a 42% (68%) efficiency for the signal with m_A of 360 (700) GeV. The same cuts are applied to b-quark jets in addition to the b identification efficiency (70%).

Events are considered as $A \to Zh \to llbb$ candidates if they contain at least two same flavour, opposite-sign leptons (e or μ) and at least 2 b jets. The di-lepton invariant mass is required to be in the range $80 < m_{ll} < 100$ GeV. Similarly, the invariant mass of the two highest-p_T b jets is demanded to be in the range $90 < m_{bb} < 140$ GeV. Finally, an additional cut is applied on the angular distance in the η–ϕ space of the b jets ($\Delta R(bb)$) for $m_A \geq 500$ GeV: $1.4 - 0.001 m_A < \Delta R(bb) < 1.8 - 0.001 m_A$.

The reconstructed mass of the A boson $m_A^{\rm rec}$ is determined as:

$$m_A^{\rm rec} \equiv m_{llbb} - m_{ll} - m_{bb} + m_Z^0 + m_h^0, \tag{4.2.1}$$

[7] ATLAS uses a right-handed coordinate system with its origin at the nominal interaction point (IP) in the centre of the detector and the z-axis along the beam pipe. The x-axis points from the IP to the centre of the LHC ring, and the y-axis points upwards. Cylindrical coordinates (r, ϕ) are used in the transverse plane, ϕ being the azimuthal angle around the beam pipe. The pseudorapidity is defined in terms of the polar angle θ as $\eta = -\ln\tan(\theta/2)$.

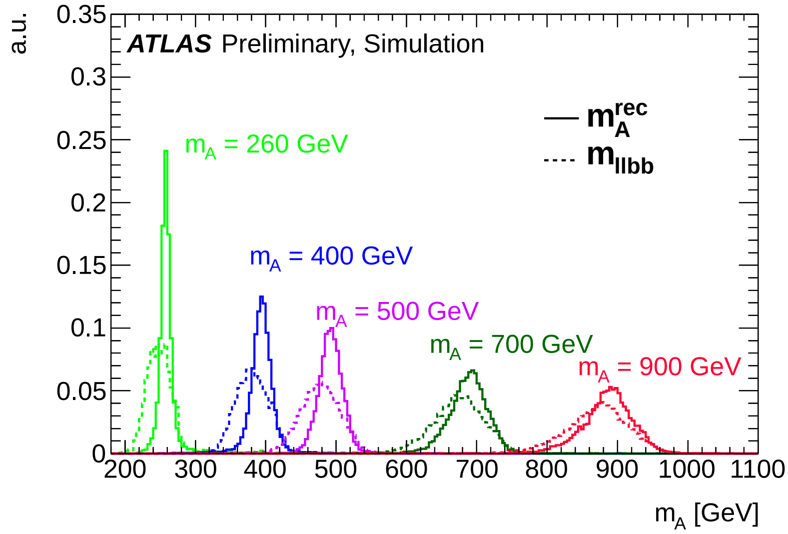

Figure 4.2.1: The reconstructed A boson mass, $m_A^{\rm rec}$, for various m_A assumptions after the full selection described in the text. The invariant mass of the two lepton and two b jet system, m_{llbb}, is also shown (dashed lines) for comparison.

where m_{llbb} is the invariant mass of the system of the two leptons and the two b jets, m_Z^0 is the nominal mass of the Z boson (91.2 GeV) and m_h^0 is the mass of the light CP-even Higgs boson which is fixed to 125 GeV. Examples of reconstructed A boson masses after the full selection are shown in Fig. 4.2.1 for some signal assumptions. In the same figure, the m_{llbb} distributions are also shown, demonstrating the improvement in the resolution obtained by the use of Eq. (4.2.1). The $m_A^{\rm rec}$ spectrum for signal and backgrounds after the full selection is shown in Fig. 4.2.2 for $m_A = 360$ and 700 GeV. In addition, the number of events for signal and background processes is shown in Table 4.2.1. In this table, the signal cross section assumption is 0.1 pb, as in the $m_A^{\rm rec}$ distributions shown in Fig. 4.2.2.

4.3 Results

The calculation of the expected sensitivity employs a binned likelihood function, which is the product over bins in the distributions of the reconstructed A mass for the signal and the background samples. The $\tilde{q}_\mu$ test statistic [74] is used to calculate 95% confidence level limits with the modified frequentist method known as CL$_{\rm s}$ [75]. For the discovery potential estimation the q_0 test statistic has been used to estimate expected 5 σ significance contours. The asympotic approximation [74] is used to evaluate the probability density functions rather

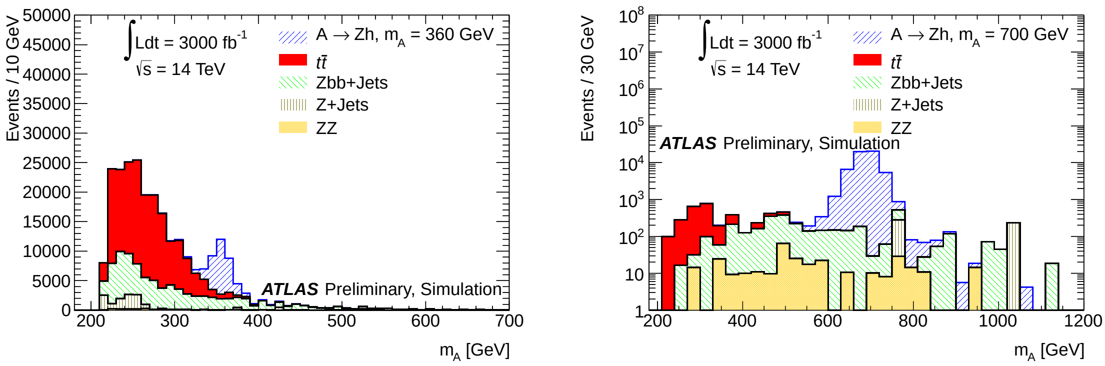

(a) (b)

Figure 4.2.2: The reconstructed A boson mass, $m_A^{\rm rec}$, is shown for signal and backgrounds after the full selection for $m_A = 360$ GeV in (a) and $m_A = 700$ GeV in (b). The signal cross section is assumed to be 0.1 pb in both cases.

Sample	$m_A = 360$ GeV	$m_A = 700$ GeV
$A \to Zh \to llbb$	2.7×10^2	5.4×10^2
$t\bar{t}$	1.4×10^5	2.2×10^3
Zbb	8.0×10^4	2.9×10^3
Z+jets	1.3×10^4	4.9×10^2
ZZ	3.0×10^3	3.1×10^2

Table 4.2.1: The number of events after all the cuts is shown for two signal mass hypotheses, $m_A = 360$ and 700 GeV. The signal cross section is assumed to be 1 fb in both cases.

than performing pseudo-experiments. The systematic uncertainties have been conservatively approximated as a 30% uncertainty, uncorrelated among the different background and signal samples.

Upper limits on the production cross section times the branching ratio $A \to Zh \to llbb$ are shown in Fig. 4.3.1. Limits on the 2HDM parameter space are shown in Figs. 4.3.2–4.3.3 in terms of constraints on the $\cos(\beta - \alpha)$ – m_A plane for given values of $\tan\beta$ and in Figs. 4.3.4–4.3.5 in terms of constraints on the $\cos(\beta - \alpha)$ – $\tan\beta$ plane for given values of m_A. Similarly, the 5 σ countour for the significance of an excess in the presence of a signal is shown in Figs. 4.3.6–4.3.9.The hashed area indicates the part of the parameter space which is inaccessible theoretically. The theory constraints considered here include Higgs potential

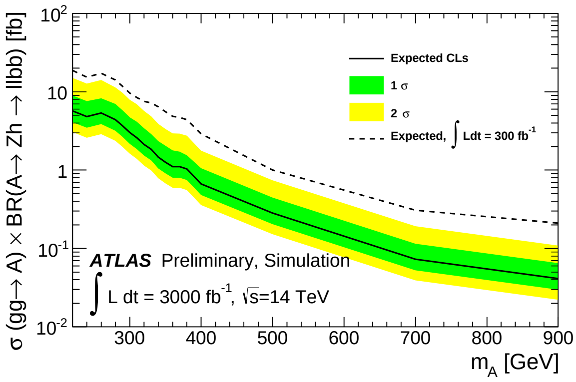

Figure 4.3.1: Expected 95% confidence level upper limits for an integrated luminosity of 300 fb^{-1} (dashed line) and 3000 fb^{-1} (solid line) on the gluon-fusion production cross section of a CP-odd Higgs boson A times its decay branching ratio to $A \to Zh \to llbb$ are presented as a function of the A boson mass, m_A. The structures in the limit seen near 260 and 370 GeV are a result of the background shape, which can be seen in the left of Fig. 4.2.2.

stability, tree-level unitarity for Higgs scattering [100] and perturbativity of the quartic Higgs boson couplings, as implemented in `2HDMC`.

This study shows that the expected 95% confidence level upper limits for the cross section times branching ratio of a gluon-fusion produced A boson decaying to $Zh \to llbb$ are in the range from 5 to 0.07 fb for the A mass range from 220 to 900 GeV and for 3000 fb^{-1}. The upper limits are 3 – 4 times larger when assuming only 300 fb^{-1} in integrated luminosity. The sensitivity in the $\cos(\beta - \alpha)$ – m_A plane reaches its maximum at $m_A \sim 340$ GeV, i.e. just below the $t\bar{t}$ decay channel threshold, and for 3000 fb^{-1}, it is up to $\cos(\beta - \alpha) \sim 0.0025$ with $\tan\beta \sim 1$ for both 2HDM types considered here. This limit is in the region where the gluon-fusion production cross section for a h boson followed by the decay into vector bosons differs from the expectation for a SM Higgs boson by less than 0.1%. The reach in the 2HDM parameter space for 300 fb^{-1} deteriorates to $\cos(\beta - \alpha) \sim 0.005$ for $m_A \sim 340$ GeV and $\tan\beta \sim 1$. Similar conclusions can be drawn for the 5 σ discovery potential, where the maximum discovery reach in $\cos(\beta - \alpha)$ is about 0.009 for $m_A \sim 340$ GeV. The sensitivity and the discovery potential with 3000 fb^{-1} are increased significantly at higher $\tan\beta$ with respect to 300 fb^{-1} due to the rapid drop of the gluon-fusion cross section as $\tan\beta$ increases (Fig. 4.1.1).

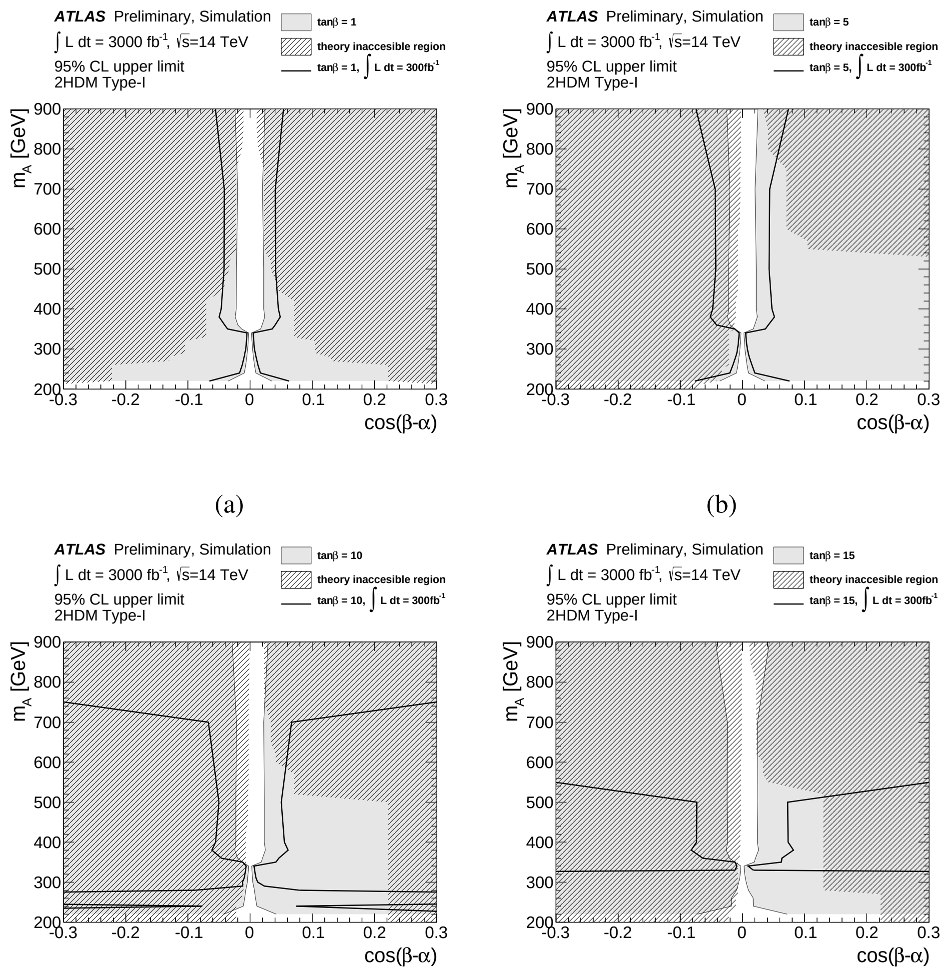

(a) (b) (c) (d)

Figure 4.3.2: The interpretation of the cross section limits shown in Fig. 4.3.1 on the $\cos(\beta - \alpha)$ – m_A plane for a type-I 2HDM. The grey area and the area contained by the black line are expected to be excluded, with 3000 fb^{-1} and 300 fb^{-1}, respectively, if no signal is present. The cases of $\tan\beta = 1$, 5, 10, and 15 are shown. The hatched area denotes the theoretically forbidden region (see text).

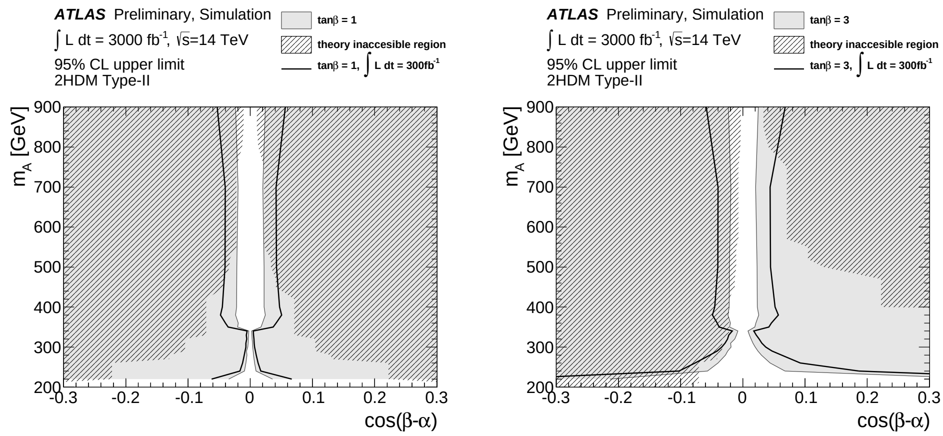

(a) (b)

Figure 4.3.3: The interpretation of the cross section limits shown in Fig. 4.3.1 on the $\cos(\beta - \alpha) - m_A$ plane for a type-II 2HDM. The grey area and the area contained by the black line are expected to be excluded, with 3000 fb^{-1} and 300 fb^{-1}, respectively, if no signal is present. The cases of $\tan\beta = 1$ and 3 are shown. The hatched area denotes the theoretically forbidden region (see text).

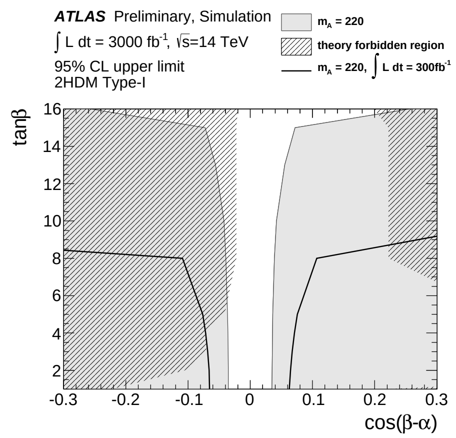

(a)

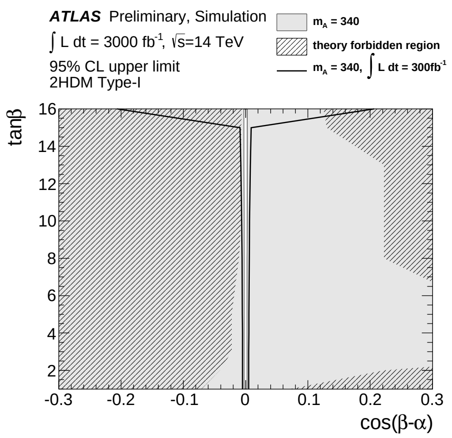

(b)

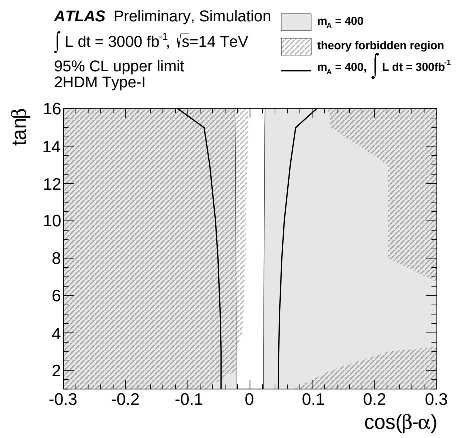

(c)

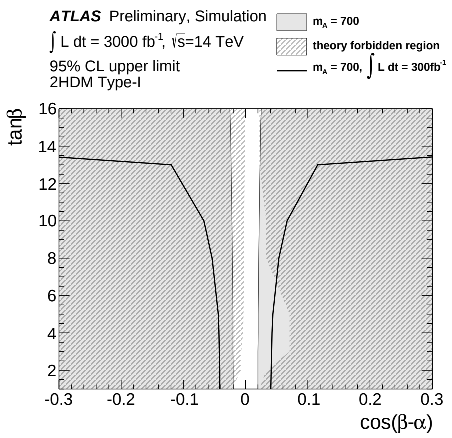

(d)

Figure 4.3.4: The interpretation of the cross section limits shown in Fig. 4.3.1 on the $\cos(\beta-\alpha)$ – $\tan\beta$ plane for a type-I 2HDM. The grey area and the area contained by the black line are expected to be excluded, with 3000 fb^{-1} and 300 fb^{-1}, respectively, if no signal is present. The cases of $m_A = 220$, 340, 400, and 700 GeV are shown. The hatched area denotes the theoretically forbidden region (see text).

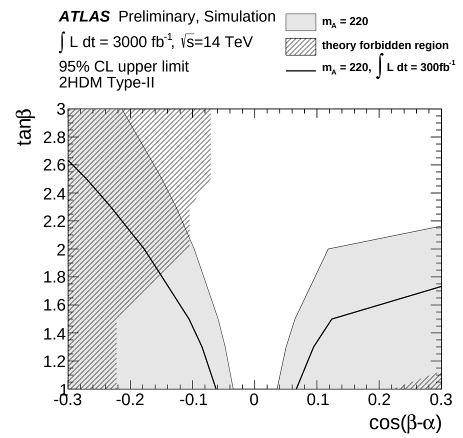

(a)

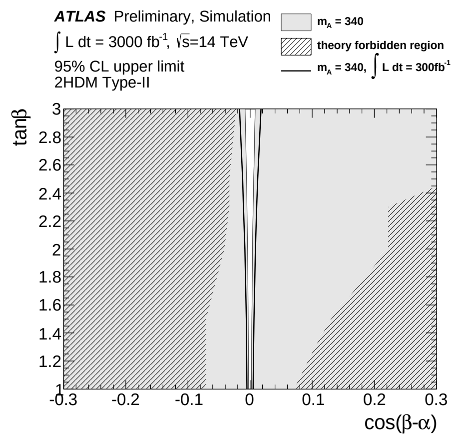

(b)

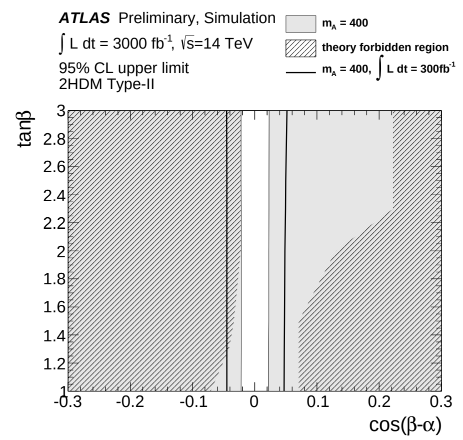

(c)

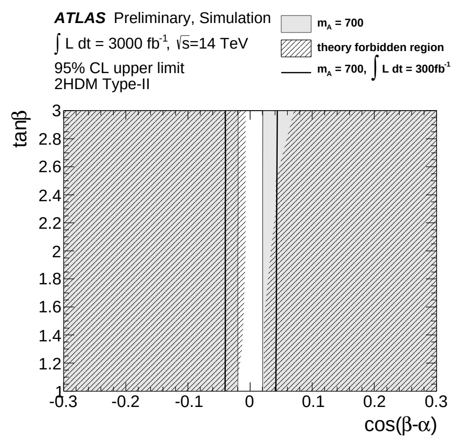

(d)

Figure 4.3.5: The interpretation of the cross section limits shown in Fig. 4.3.1 on the $\cos(\beta - \alpha) - m_A$ plane for a type-II 2HDM. The grey area and the area contained by the black line are expected to be excluded, with 3000 fb^{-1} and 300 fb^{-1}, respectively, if no signal is present. The cases of $m_A = 220$, 340, 400, and 700 GeV are shown. The hatched area denotes the theoretically forbidden region (see text).

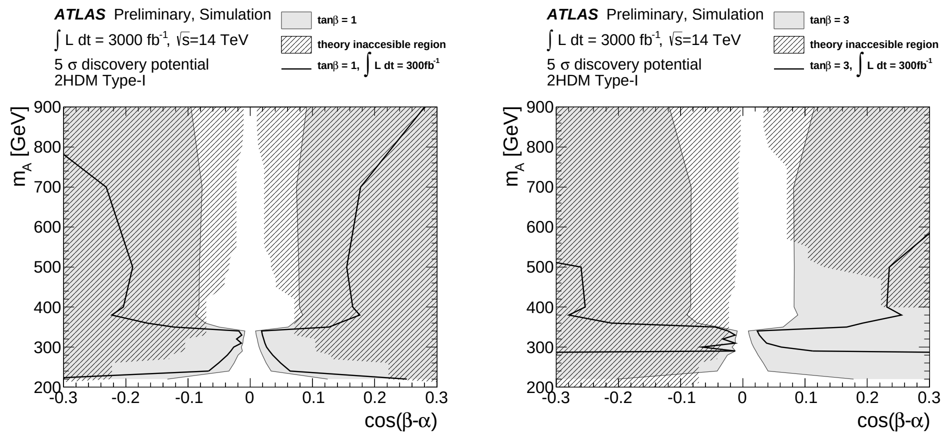

(a) (b)

Figure 4.3.6: The discovery potential with 3000 and 300 fb^{-1} of integrated luminosity for a type-I 2HDM. The grey area and the area contained by the black line indicated the regions where a significance of at least 5 σ is expected, with 3000 fb^{-1} and 300 fb^{-1}, respectively, if a signal is present. The cases of $\tan\beta = 1$ and 3 are shown. The hatched area denotes the theoretically forbidden region (see text).

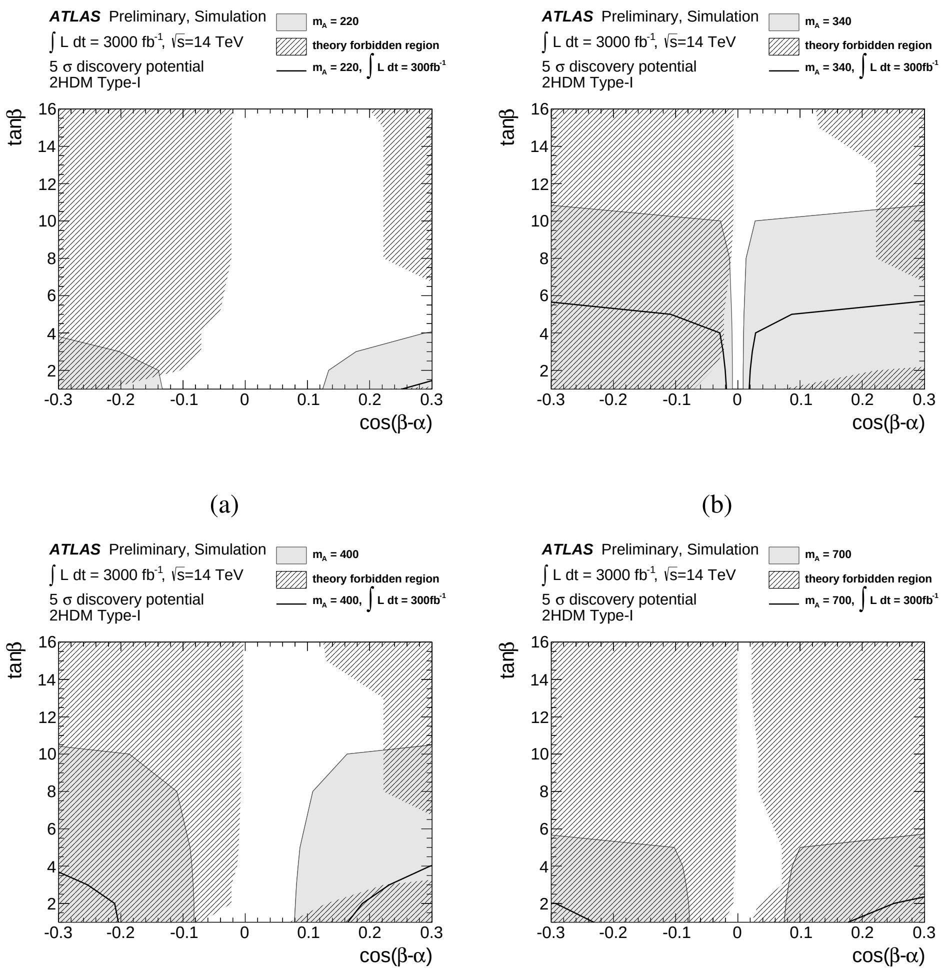

(a) (b)

(c) (d)

Figure 4.3.7: The discovery potential with 3000 and 300 fb^{-1} of integrated luminosity for a type-I 2HDM. The grey area and the area contained by the black line indicated the regions where a significance of at least 5 σ is expected, with 3000 fb^{-1} and 300 fb^{-1}, The cases of m_A = 220, 340, 400, and 700 GeV are shown. The hatched area denotes the theoretically forbidden region (see text).

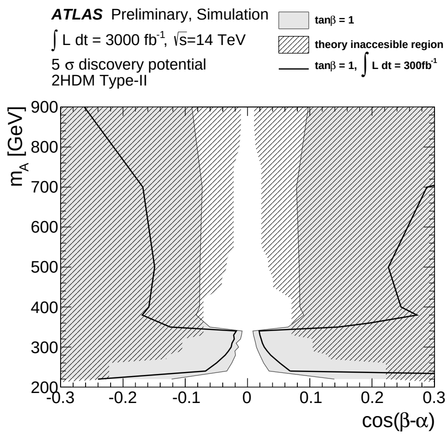

(a)

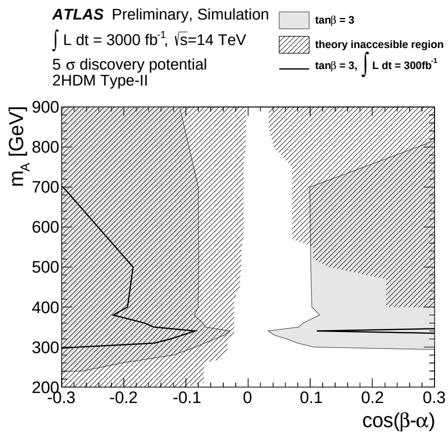

(b)

Figure 4.3.8: The discovery potential with 3000 and 300 fb^{-1} of integrated luminosity for a type-II 2HDM. The grey area and the area contained by the black line indicated the regions where a significance of at least 5 σ is expected, with 3000 fb^{-1} and 300 fb^{-1}, respectively, if a signal is present. The cases of $\tan\beta = 1$ and 3 are shown. The hatched area denotes the theoretically forbidden region (see text).

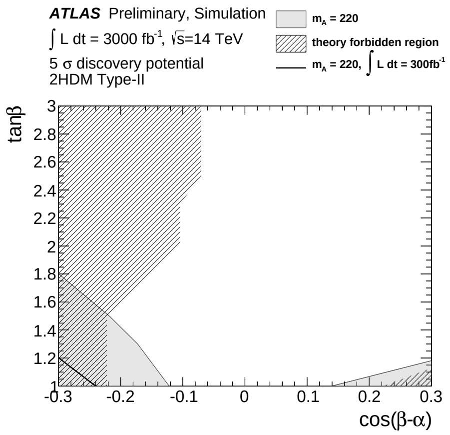

(a)

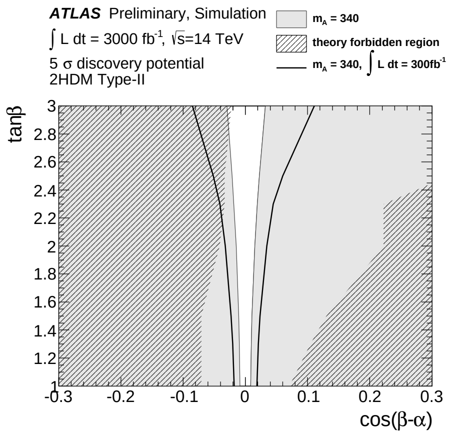

(b)

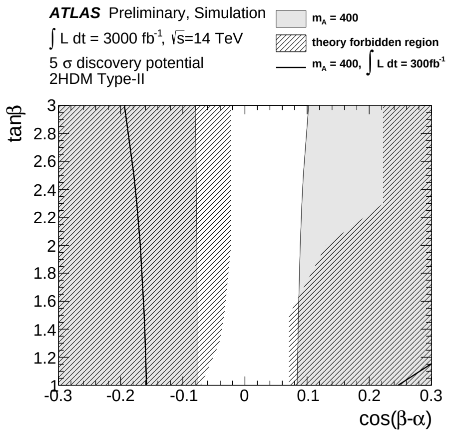

(c)

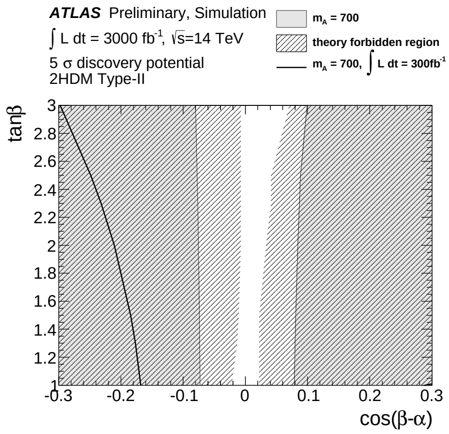

(d)

Figure 4.3.9: The discovery potential with 3000 and 300 fb^{-1} of integrated luminosity for a type-II 2HDM. The grey area and the area contained by the black line indicated the regions where a significance of at least 5 σ is expected, with 3000 fb^{-1} and 300 fb^{-1}, The cases of $m_A = 220$, 340, 400, and 700 GeV are shown. The hatched area denotes the theoretically forbidden region (see text).

4.4 Conclusions

The studies reported here have investigated the ATLAS sensitivity to various signatures for beyond-SM Higgs bosons using datasets corresponding to integrated luminosities of 300 fb^{-1} and 3000 fb^{-1} at $\sqrt{s} = 14$ TeV. A 2HDM-motivated scenario has been examined, in which a gluon-fusion produced CP-odd Higgs boson, A, decays to $A \to Zh \to llbb$. Sensitivities to cross sections times branching ratios from 5 to 0.07 fb for an A mass in the range from 220 to 900 GeV have been reported for an integrated luminosity of 3000 fb^{-1}. The results obtained are improved by a factor of 3 to 4 with respect to the upper limit assuming 300 fb^{-1}.

5 Summary

In this thesis I summarize my work in investigating the nature of the SM-like Higgs Boson within the framework of BSM and future prospects for High luminosity (**HL**) LHC.

Three analyses were performed:

- Search for light charged Higgs in ATLAS (Section 2), the upper limits results on the branching fraction $\mathcal{B}(t \to bH^+)$ are shown in Fig. 2.7.1. To the best of our knowledge, this is the only analysis of this sort.
- Expectations of the leptonic yukawa coupling of the HL-LHC (Section 3), the study is summarized in Fig. 3.5.1.
- Prospects for pseudoscalar decays at the HL-LHC (Section 4), the sensitivity can be found in Fig. 4.3.1.

Though the HL-LHC studies are only predictions, they are already used to design the future experimental strategy, in particular in the ongoing debates between HL-LHC and various prospective linear colliders.

To conclude, this thesis expanded both the current understanding of HEP and the future prospectives.

6 References

[1] **ATLAS** Collaboration, *Observation of a new particle in the search for the Standard Model Higgs boson with the ATLAS detector at the LHC*, *Phys.Lett.* **B716** (2012) 1–29, [arXiv:1207.7214].

[2] **CMS** Collaboration, *Observation of a new boson at a mass of 125 GeV with the CMS experiment at the LHC*, *Phys.Lett.* **B716** (2012) 30–61, [arXiv:1207.7235].

[3] F. Englert and R. Brout, *Broken Symmetry and the Mass of Gauge Vector Mesons*, *Phys.Rev.Lett.* **13** (1964) 321–323.

[4] P. W. Higgs, *Broken symmetries, massless particles and gauge fields*, *Phys.Lett.* **12** (1964) 132–133.

[5] P. W. Higgs, *Broken Symmetries and the Masses of Gauge Bosons*, *Phys.Rev.Lett.* **13** (1964) 508–509.

[6] **ATLAS** Collaboration, *Search for charged Higgs bosons decaying via $H^+ \to \tau\nu$ in top quark pair events using pp collision data at $\sqrt{s} = 7$ TeV with the ATLAS detector*, *JHEP* **1206** (2012) 039, [arXiv:1204.2760].

[7] **ATLAS** Collaboration, *Physics at a High-Luminosity LHC with ATLAS (Update)*, *ATL-PHYS-PUB-2012-004*.

[8] **ATLAS** Collaboration, *Beyond Standard Model Higgs boson searches at a High-Luminosity LHC with ATLAS*, *ATL-PHYS-PUB-2013-016*.

[9] S. Glashow, *Partial Symmetries of Weak Interactions*, *Nucl.Phys.* **22** (1961) 579–588.

[10] S. Weinberg, *A Model of Leptons*, *Phys.Rev.Lett.* **19** (1967) 1264–1266.

[11] A. Salam, *Weak and Electromagnetic Interactions*, *Conf.Proc.* **C680519** (1968) 367–377.

[12] G. Guralnik, C. Hagen, and T. Kibble, *Global Conservation Laws and Massless Particles*, *Phys.Rev.Lett.* **13** (1964) 585–587.

[13] P. W. Higgs, *Spontaneous Symmetry Breakdown without Massless Bosons*, *Phys.Rev.* **145** (1966) 1156–1163.

[14] T. Kibble, *Symmetry breaking in nonAbelian gauge theories*, *Phys.Rev.* **155** (1967) 1554–1561.

[15] T. Schwetz, *Neutrino oscillations: Present status and outlook*, *AIP Conf.Proc.* **981** (2008) 8–12, [`arXiv:0710.5027`].

[16] A. Strumia and F. Vissani, *Neutrino masses and mixings and...*, `hep-ph/0606054`.

[17] J. Einasto, *Dark Matter*, `arXiv:0901.0632`.

[18] P. Huet, *Electroweak baryogenesis and the standard model*, `hep-ph/9406301`.

[19] S. Davidson, E. Nardi, and Y. Nir, *Leptogenesis*, *Phys.Rept.* **466** (2008) 105–177, [`arXiv:0802.2962`].

[20] G. Branco, P. Ferreira, L. Lavoura, M. Rebelo, M. Sher, et al., *Theory and phenomenology of two-Higgs-doublet models*, *Phys.Rept.* **516** (2012) 1–102, [`arXiv:1106.0034`].

[21] P. Fayet, *Supersymmetry and Weak, Electromagnetic and Strong Interactions*, *Phys.Lett.* **B64** (1976) 159.

[22] P. Fayet, *Spontaneously Broken Supersymmetric Theories of Weak, Electromagnetic and Strong Interactions*, *Phys.Lett.* **B69** (1977) 489.

[23] G. R. Farrar and P. Fayet, *Phenomenology of the Production, Decay, and Detection of New Hadronic States Associated with Supersymmetry*, *Phys.Lett.* **B76** (1978) 575–579.

[24] P. Fayet, *Relations Between the Masses of the Superpartners of Leptons and Quarks, the Goldstino Couplings and the Neutral Currents*, *Phys.Lett.* **B84** (1979) 416.

[25] S. Dimopoulos and H. Georgi, *Softly Broken Supersymmetry and SU(5)*, *Nucl.Phys.* **B193** (1981) 150.

[26] M. Trodden, *Electroweak baryogenesis: A Brief review*, `hep-ph/9805252`.

[27] M. Joyce, T. Prokopec, and N. Turok, *Nonlocal electroweak baryogenesis. Part 2: The Classical regime*, *Phys.Rev.* **D53** (1996) 2958–2980, [hep-ph/9410282].

[28] A. Djouadi, *The Anatomy of electro-weak symmetry breaking. II. The Higgs bosons in the minimal supersymmetric model*, *Phys.Rept.* **459** (2008) 1–241, [hep-ph/0503173].

[29] L. Evans and P. Bryant, *LHC Machine*, *JINST* **3** (2008) S08001.

[30] **ATLAS** Collaboration, *The ATLAS Experiment at the CERN Large Hadron Collider*, *JINST* **3** (2008) S08003.

[31] J. F. Gunion, H. E. Haber, G. L. Kane, and S. Dawson, *The Higgs Hunter's Guide*, *Front.Phys.* **80** (2000) 1–448.

[32] J. F. Gunion, H. E. Haber, G. L. Kane, and S. Dawson, *Errata for the Higgs hunter's guide*, hep-ph/9302272.

[33] J. Gunion and H. E. Haber, *Higgs Bosons in Supersymmetric Models. 1.*, *Nucl.Phys.* **B272** (1986) 1.

[34] **LHC Higgs Cross Section Working Group** Collaboration, *Handbook of LHC Higgs Cross Sections: 1. Inclusive Observables*, arXiv:1101.0593.

[35] **LEP Higgs Working Group for Higgs boson searches** Collaboration, *Search for charged Higgs bosons: Preliminary combined results using LEP data collected at energies up to 209-GeV*, hep-ex/0107031.

[36] **CDF** Collaboration, *Search for charged Higgs bosons in decays of top quarks in p anti-p collisions at* $\sqrt{s} = 1.96$ *TeV*, *Phys.Rev.Lett.* **103** (2009) 101803, [arXiv:0907.1269].

[37] **D0** Collaboration, *Search for charged Higgs bosons in top quark decays*, *Phys.Lett.* **B682** (2009) 278–286, [arXiv:0908.1811].

[38] **CMS** Collaboration, *H+* $\rightarrow$ *gt; Tau in Top quark decays*, *CMS-PAS-HIG-11-008* (2011).

[39] **ATLAS** Collaboration, *Search for Charged Higgs Bosons in the τ+jets Final State in $t\bar{t}$ Decays with 1.03 fb^{-1} of pp Collision Data Recorded at $\sqrt{s} = 7$ TeV with the ATLAS Experiment*, *ATLAS-CONF-2011-138* (2011).

[40] **ATLAS** Collaboration, *Search for a charged Higgs boson decaying via H+ to tau(lep)+nu in ttbar events with one or two light leptons in the final state using 1.03/fb of pp collision data recorded at sqrt(s) = 7 TeV with the ATLAS detector*, *ATLAS-CONF-2011-151* (2011).

[41] **ATLAS** Collaboration, *Measurement of the W boson polarisation in top quark decays in 0.70 fb^{-1} of pp collisions at sqrt(s)=7 TeV with the ATLAS detector*, *ATLAS-CONF-2011-122* (2011).

[42] E. Gross and O. Vitells, *Transverse mass observables for charged Higgs boson searches at hadron colliders*, *Phys.Rev.* **D81** (2010) 055010, [arXiv:0907.5367].

[43] S. Frixione and B. R. Webber, *Matching NLO QCD computations and parton shower simulations*, *JHEP* **0206** (2002) 029, [hep-ph/0204244].

[44] B. P. Kersevan and E. Richter-Was, *The Monte Carlo event generator AcerMC versions 2.0 to 3.8 with interfaces to PYTHIA 6.4, HERWIG 6.5 and ARIADNE 4.1*, *Comput.Phys.Commun.* **184** (2013) 919–985, [hep-ph/0405247].

[45] H.-L. Lai, M. Guzzi, J. Huston, Z. Li, P. M. Nadolsky, et al., *New parton distributions for collider physics*, *Phys.Rev.* **D82** (2010) 074024, [arXiv:1007.2241].

[46] G. Corcella, I. Knowles, G. Marchesini, S. Moretti, K. Odagiri, et al., *HERWIG 6: An Event generator for hadron emission reactions with interfering gluons (including supersymmetric processes)*, *JHEP* **0101** (2001) 010, [hep-ph/0011363].

[47] J. Butterworth, J. R. Forshaw, and M. Seymour, *Multiparton interactions in photoproduction at HERA*, *Z.Phys.* **C72** (1996) 637–646, [hep-ph/9601371].

[48] T. Sjostrand, S. Mrenna, and P. Z. Skands, *PYTHIA 6.4 Physics and Manual*, *JHEP* **0605** (2006) 026, [hep-ph/0603175].

[49] M. Aliev, H. Lacker, U. Langenfeld, S. Moch, P. Uwer, et al., *HATHOR: HAdronic Top and Heavy quarks crOss section calculatoR*, *Comput.Phys.Commun.* **182** (2011) 1034–1046, [arXiv:1007.1327].

[50] N. Kidonakis, *Next-to-next-to-leading-order collinear and soft gluon corrections for t-channel single top quark production*, *Phys.Rev.* **D83** (2011) 091503, [arXiv:1103.2792].

[51] N. Kidonakis, *NNLL resummation for s-channel single top quark production*, *Phys.Rev.* **D81** (2010) 054028, [arXiv:1001.5034].

[52] N. Kidonakis, *Two-loop soft anomalous dimensions for single top quark associated production with a W- or H-*, *Phys.Rev.* **D82** (2010) 054018, [arXiv:1005.4451].

[53] S. Frixione, E. Laenen, P. Motylinski, and B. R. Webber, *Single-top production in MC@NLO*, *JHEP* **0603** (2006) 092, [hep-ph/0512250].

[54] S. Frixione, P. Nason, and C. Oleari, *Matching NLO QCD computations with Parton Shower simulations: the POWHEG method*, *JHEP* **0711** (2007) 070, [arXiv:0709.2092].

[55] J. Pumplin, D. Stump, J. Huston, H. Lai, P. M. Nadolsky, et al., *New generation of parton distributions with uncertainties from global QCD analysis*, *JHEP* **0207** (2002) 012, [hep-ph/0201195].

[56] J. Alwall, S. Hoche, F. Krauss, N. Lavesson, L. Lonnblad, et al., *Comparative study of various algorithms for the merging of parton showers and matrix elements in hadronic collisions*, *Eur.Phys.J.* **C53** (2008) 473–500, [arXiv:0706.2569].

[57] R. Gavin, Y. Li, F. Petriello, and S. Quackenbush, *W Physics at the LHC with FEWZ 2.1*, *Comput.Phys.Commun.* **184** (2013) 208–214, [arXiv:1201.5896].

[58] R. Gavin, Y. Li, F. Petriello, and S. Quackenbush, *FEWZ 2.0: A code for hadronic Z production at next-to-next-to-leading order*, *Comput.Phys.Commun.* **182** (2011) 2388–2403, [arXiv:1011.3540].

[59] J. M. Campbell, R. K. Ellis, and C. Williams, *Vector boson pair production at the LHC*, *JHEP* **1107** (2011) 018, [arXiv:1105.0020].

[60] Z. Was and P. Golonka, *TAUOLA as tau Monte Carlo for future applications*, *Nucl.Phys.Proc.Suppl.* **144** (2005) 88–94, [hep-ph/0411377].

[61] E. Barberio, B. van Eijk, and Z. Was, *PHOTOS: A Universal Monte Carlo for QED radiative corrections in decays*, *Comput.Phys.Commun.* **66** (1991) 115–128.

[62] **ATLAS** Collaboration, *ATLAS tunes of PYTHIA 6 and Pythia 8 for MC11*, *ATL-PHYS-PUB-2011-009* (2011).

[63] **ATLAS** Collaboration, *New ATLAS event generator tunes to 2010 data*, *ATL-PHYS-PUB-2011-008* (2011).

[64] **GEANT4** Collaboration, S. Agostinelli et al., *GEANT4: A Simulation toolkit*, *Nucl.Instrum.Meth.* **A506** (2003) 250–303.

[65] **ATLAS** Collaboration, *The ATLAS Simulation Infrastructure*, *Eur.Phys.J.* **C70** (2010) 823–874, [arXiv:1005.4568].

[66] **ATLAS** Collaboration, *Luminosity Determination in pp Collisions at sqrt(s) = 7 TeV using the ATLAS Detector in 2011*, *ATLAS-CONF-2011-116* (2011).

[67] **ATLAS** Collaboration, *Data-Quality Requirements and Event Cleaning for Jets and Missing Transverse Energy Reconstruction with the ATLAS Detector in Proton-Proton Collisions at a Center-of-Mass Energy of $sqrts = 7$ TeV*, *ATLAS-CONF-2010-038* (2010).

[68] M. Cacciari, G. P. Salam, and G. Soyez, *The Anti-k(t) jet clustering algorithm*, *JHEP* **0804** (2008) 063, [arXiv:0802.1189].

[69] M. Cacciari and G. P. Salam, *Dispelling the N^3 myth for the k_t jet-finder*, *Phys.Lett.* **B641** (2006) 57–61, [hep-ph/0512210].

[70] **ATLAS** Collaboration, *Jet energy scale and its systematic uncertainty in proton-proton collisions at sqrt(s)=7 TeV in ATLAS 2010 data*, *ATLAS-CONF-2011-032* (2011).

[71] **D0** Collaboration, *Measurement of the $p\bar{p} \to t\bar{t}$ production cross section at $\sqrt{s}$ = 1.96-TeV in the fully hadronic decay channel.*, *Phys.Rev.* **D76** (2007) 072007, [hep-ex/0612040].

[72] **ATLAS** Collaboration, *Commissioning of the ATLAS high-performance b-tagging algorithms in the 7 TeV collision data*, *ATLAS-CONF-2011-102* (2011).

[73] **ATLAS** Collaboration, *Performance of the Reconstruction and Identification of Hadronic Tau Decays with ATLAS*, *ATLAS-CONF-2011-152* (2011).

[74] G. Cowan, K. Cranmer, E. Gross, and O. Vitells, *Asymptotic formulae for likelihood-based tests of new physics*, *Eur.Phys.J.* **C71** (2011) 1554, [arXiv:1007.1727].

[75] A. L. Read, *Presentation of search results: The CL(s) technique*, *J.Phys.* **G28** (2002) 2693–2704.

[76] M. S. Carena, S. Heinemeyer, C. Wagner, and G. Weiglein, *Suggestions for benchmark scenarios for MSSM Higgs boson searches at hadron colliders*, *Eur.Phys.J.* **C26** (2003) 601–607, [hep-ph/0202167].

[77] **LHC Higgs Cross Section Working Group** Collaboration, *Handbook of LHC Higgs Cross Sections: 2. Differential Distributions*, arXiv:1201.3084.

[78] M. S. Carena, D. Garcia, U. Nierste, and C. E. Wagner, *Effective Lagrangian for the $\bar{t}bH^+$ interaction in the MSSM and charged Higgs phenomenology*, *Nucl.Phys.* **B577** (2000) 88–120, [hep-ph/9912516].

[79] H. E. Logan and D. MacLennan, *Charged Higgs phenomenology in the flipped two Higgs doublet model*, *Phys.Rev.* **D81** (2010) 075016, [arXiv:1002.4916].

[80] **European Strategy for Particle Physics Preparatory Group** Collaboration, *Physics Briefing Book: Input for the Strategy Group to draft the update of the European Strategy for Particle Physics*, *CERN-ESG-005* (2013).

[81] **ALICE** Collaboration, *Upgrade of the ALICE Experiment: Letter Of Intent*, *J.Phys.* **G41** (2014) 087001.

[82] **ATLAS** Collaboration, *Performance assumptions based on full simulation for an upgraded ATLAS detector at a High-Luminosity LHC*, Tech. Rep. ATL-PHYS-PUB-2013-009, CERN, Geneva, 2013.

[83] LHC Higgs Cross-section Working Group. http://twiki.cern.ch/twiki/bin/view/LHCPhysics/SMInputParameter.

[84] **ATLAS** Collaboration, *Search for the Standard Model Higgs boson in the H to $\tau^+\tau^-$ decay mode in $\sqrt{s} = 7$ TeV pp collisions with ATLAS*, *JHEP* **1209** (2012) 070, [`arXiv:1206.5971`].

[85] J. F. Gunion and X.-G. He, *Determining the CP nature of a neutral Higgs boson at the LHC*, *Phys.Rev.Lett.* **76** (1996) 4468–4471, [`hep-ph/9602226`].

[86] **ATLAS** Collaboration, *Coupling properties of the new Higgs-like boson observed with the ATLAS detector at the LHC*, *ATLAS-CONF-2012-127* (2012).

[87] **ATLAS** Collaboration, *Measurements of Higgs boson production and couplings in diboson final states with the ATLAS detector at the LHC*, *Phys.Lett.* **B726** (2013) 88–119, [`arXiv:1307.1427`].

[88] **ATLAS** Collaboration, *Evidence for the spin-0 nature of the Higgs boson using ATLAS data*, *Phys.Lett.* **B726** (2013) 120–144, [`arXiv:1307.1432`].

[89] R. V. Harlander, S. Liebler, and H. Mantler, *SusHi: A program for the calculation of Higgs production in gluon fusion and bottom-quark annihilation in the Standard Model and the MSSM*, *Computer Physics Communications* **184** (2013) 1605–1617, [`arXiv:1212.3249`].

[90] **ATLAS** Collaboration, *Search for the neutral Higgs bosons of the Minimal Supersymmetric Standard Model in pp collisions at $\sqrt{s} = 7$ TeV with the ATLAS detector*, *JHEP* **1302** (2013) 095, [`arXiv:1211.6956`].

[91] **CMS** Collaboration, *Search for MSSM Neutral Higgs Bosons Decaying to Tau Pairs in pp Collisions*, *CMS-PAS-HIG-12-050* (2012).

[92] **CMS** Collaboration, *Search for Neutral MSSM Higgs Bosons in the mu+mu- final state with the CMS experiment in pp Collisions at sqrt s =7 TeV*, *CMS-PAS-HIG-12-011* (2012).

[93] D. Eriksson, J. Rathsman, and O. Stal, *2HDMC: Two-Higgs-Doublet Model Calculator Physics and Manual*, *Comput.Phys.Commun.* **181** (2010) 189–205, [arXiv:0902.0851].

[94] J. Alwall, M. Herquet, F. Maltoni, O. Mattelaer, and T. Stelzer, *MadGraph 5 : Going Beyond*, *JHEP* **1106** (2011) 128, [arXiv:1106.0522].

[95] T. Sjostrand, S. Mrenna, and P. Z. Skands, *A Brief Introduction to PYTHIA 8.1*, *Comput.Phys.Commun.* **178** (2008) 852–867, [arXiv:0710.3820].

[96] M. L. Mangano, M. Moretti, F. Piccinini, R. Pittau, and A. D. Polosa, *ALPGEN, a generator for hard multiparton processes in hadronic collisions*, *JHEP* **0307** (2003) 001, [hep-ph/0206293].

[97] K. Melnikov and F. Petriello, *Electroweak gauge boson production at hadron colliders through O(alpha(s)**2)*, *Phys.Rev.* **D74** (2006) 114017, [hep-ph/0609070].

[98] J. M. Campbell and R. Ellis, *MCFM for the Tevatron and the LHC*, *Nucl.Phys.Proc.Suppl.* **205-206** (2010) 10–15, [arXiv:1007.3492].

[99] **ATLAS** Collaboration, *Search for the bb decay of the Standard Model Higgs boson in associated W/ZH production with the ATLAS detector*, *ATLAS-CONF-2013-079* (2013).

[100] I. Ginzburg and I. Ivanov, *Tree-level unitarity constraints in the most general 2HDM*, *Phys.Rev.* **D72** (2005) 115010, [hep-ph/0508020].

Acknowledgments

I am grateful to my advisor, Prof. Eilam Gross, for giving me the opportunity to be his student, for all of his suggestions and dedicated guidance throughout this work and of course for his support. He definitely made me the best student I can be!

Also, I would like to thank my PhD advisory committee, Prof. Yossi Nir and Prof. Erez Etzion, for pushing me to know more, learn more and have better understanding.

I also want to thank Ami Shalit and the Feinberg Graduate School for allowing me to follow my wishes. I would like to thank the HEP group in Weizmann who helped me along the way, especially Giora Mikenberg, Ehud Duchovni, Ohad Silbert, Raz Alon, Gal Dadiani, Ofer Vitells, Yotam Soreq and Aielet Efrati. And last but not least, I would like to thank GOD. I know that during all the way, I wasn't alone.

This work is of course the outcome of the endless support I always got from my family. My parents, Itzhak and Orit Zada, who were always (since I was a kid) behind me, supporting me and proud of me.

My children Yair and Yahav who made this period full of joy, deserve a special thank.

In the end, I would specially like to thank my dearest husband David for the endless love, support, encouragement and help!